Volume 11
Number 4
21 February 2024
Pages 865–1110

Materials Horizons

rsc.li/materials-horizons

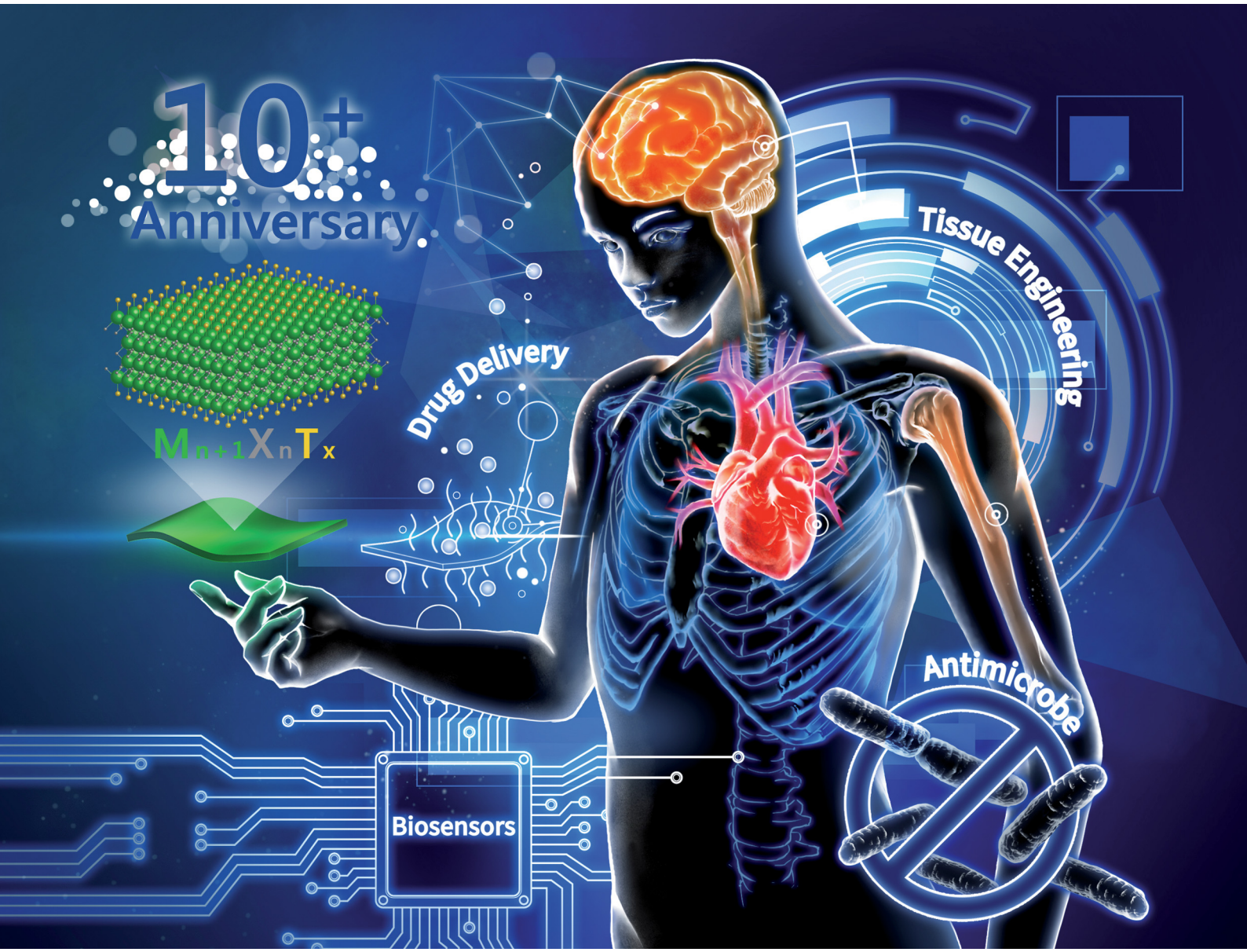

ISSN 2051-6347

ROYAL SOCIETY OF CHEMISTRY

REVIEW ARTICLE
I-Chi Lee, Yi-Chen Ethan Li, Mei-Hwa Lee, Hung-Yin Lin *et al.*
Recent advances using MXenes in biomedical applications

10 YEARS ANNIVERSARY

Materials Horizons

ROYAL SOCIETY OF CHEMISTRY

REVIEW

View Article Online
View Journal | View Issue

Cite this: *Mater. Horiz.*, 2024, **11**, 876

Recent advances using MXenes in biomedical applications

I-Chi Lee, †*[a] Yi-Chen Ethan Li,†*[b] James L. Thomas,[c] Mei-Hwa Lee*[d] and Hung-Yin Lin *[e]

Received 30th September 2023,
Accepted 1st December 2023

DOI: 10.1039/d3mh01588b

rsc.li/materials-horizons

An MXene is a novel two-dimensional transition metal carbide or nitride, with a typical formula of $M_{n+1}X_nT_x$ (M = transition metals, X = carbon or nitrogen, and T = functional groups). MXenes have found wide application in biomedicine and biosensing, owing to their high biocompatibility, abundant reactive surface groups, good conductivity, and photothermal properties. Applications include photo- and electrochemical sensors, energy storage, and electronics. This review will highlight recent applications of MXene and MXene-derived materials in drug delivery, tissue engineering, antimicrobial activity, and biosensors (optical and electrochemical). We further elaborate on recent developments in utilizing MXenes for photothermal cancer therapy, and we explore multimodal treatments, including the integration of chemotherapeutic agents or magnetic nanoparticles for enhanced therapeutic efficacy. The high surface area and reactivity of MXenes provide an interface to respond to the changes in the environment, allowing MXene-based drug carriers to respond to changes in pH, reactive oxygen species (ROS), and electrical signals for controlled release applications. Furthermore, the conductivity of MXene enables it to provide electrical stimulation for cultured cells and endows it with photocatalytic capabilities that can be used in antibiotic applications. Wearable and *in situ* sensors incorporating MXenes are also included. Major challenges and future development directions of MXenes in biomedical applications are also discussed. The remarkable properties of MXenes will undoubtedly lead to their increasing use in the applications discussed here, as well as many others.

Wider impact

An MXene is a novel two-dimensional transition metal carbide or nitride characterized by high biocompatibility, abundant reactive surface groups, good conductivity, and photothermal properties. Since the first synthesis in 2011, MXenes have undergone more than a decade of development. MXene-based materials find widespread application in photo- and electrochemical sensors, energy storage, and electronics. In the past five years, the high biocompatibility of MXene has been confirmed, leading to a growing interest in the applications of MXene-based materials in biomedicine and biosensing. This comprehensive review aims to elucidate recent advancements in the application of MXene and MXene-derived materials within the regions of drug delivery, tissue engineering, antimicrobial activity, and biosensors. Additionally, we will address current challenges and explore prospective directions for the biomedical application of MXene-based materials. In this review, we posit that the exceptional properties of MXene-based materials will undoubtedly facilitate their increasing integration into smart delivery systems, bioactuators, biosensors, and various other technologies within the realm of future biomedical applications.

1. Introduction

MXenes are a family of two-dimensional (2D) nanomaterials with a carbide or nitride layer (X layer) sandwiched between transition metal layers (M-layers); with more than 100 unique stoichiometric MXene combinations discovered to date, these nanomaterials can achieve wide tunability by varying the ratios of M or X layers.[1] MAX phases of MXenes are layered, hexagonal

[a] *Department of Biomedical Engineering and Environmental Sciences, National Tsing Hua University, Hsinchu, 300044, Taiwan*
[b] *Department of Chemical Engineering, Feng Chia University, Taichung, 40724, Taiwan*
[c] *Department of Physics and Astronomy, University of New Mexico, Albuquerque, NM 87131, USA*
[d] *Department of Materials Science and Engineering, I-Shou University, Kaohsiung 84001, Taiwan*
[e] *Department of Chemical and Materials Engineering, National University of Kaohsiung, 700, Kaohsiung University Rd., Nan-Tzu District, Kaohsiung 81148, Taiwan. E-mail: linhy@ntu.edu.tw, linhy@caa.columbia.edu; Tel: +886(7)591-9455, +886(912)178-751*
† Both authors contributed equally to this manuscript.

carbides and nitrides with the general formula $M_{n+1}AX_n$, (MAX) where n = 1 to 4, M is an early transition metal, A is an A-group element (mostly IIIA and IVA, or groups 13 and 14) and X is either carbon or nitrogen.[2] The layered structure consists of edge-sharing, distorted XM_6 octahedra interleaved by single planar layers of the A-group element.[2]

MXenes have found wide application in biological research and biosensing, owing to their high biocompatibility, abundant reactive surface groups, good conductivity, and photothermal properties.[3] Chen *et al.* comprehensively reviewed the applications of MXenes in the biological field, including biosensing, antibacterial activity, reactive oxygen species (ROS) and free radical scavenging, tissue repair and antitumor therapy.[3] Garg and Vitale, in their recent review, highlighted the emerging biomedical applications of MXenes with specific emphasis on bioelectronics, biosensors, tissue engineering, and therapeutics.[4] Miao *et al.* also reviewed the fabrication, modification and biomedical applications of MXene; MXene/carbon composites were also discussed, focusing on their biomedical applications, such as biosensors, antibacterial materials, drug delivery, and the diagnosis and treatment of diseases.[5] This review will focus on four rapidly expanding fields of MXene biomedical applications: drug delivery, tissure engineering, antimicrobial activity, and biosensing (Fig. 1).

The unique properties of MXenes, such as their metal-like electrical conductivity reaching $\approx$20 000 S cm^{-1}, render them quite useful in a large number of applications, including energy storage, communications, and optoelectronic, biomedical, and environmental applications.[6] The first MXene was synthesized by selectively etching metal layers from the MAX phases

I-Chi Lee

Prof. Lee is currently an Associate professor at the Department of Biomedical Engineering and Environmental Sciences, National Tsing Hua University. Dr I Chi Lee received her PhD from the Department of Biomedical Engineering, National Taiwan University, in 2007. She then worked as a postdoctoral research fellow at the genomics research center, Academia Sinica in Taiwan, and finally served as a Professor at Chang Gung University. She has published over 60 peer-reviewed articles and received multiple important research awards in Taiwan, including Ta-You Wu Memorial award in 2018. Her research focuses on biomaterials, tissue engineering, stem cells application and drug delivery.

Yi-Chen Ethan Li

Yi-Chen Ethan Li is a faculty in the Department of Chemical Engineering at Feng Chia University. His scientific interests include the fundamental research of tissue engineering, developing artificial tissues/organs and organs-on-chips models via 3D bioprinting and microfluidic technologies. Through this research, he wants to further apply the theories from fundamental research and the developed models to the applications of drug testing/screening, developmental biology, biosensors, and regenerative medicine.

James L. Thomas

James L Thomas earned a BS degree in physics from Stanford University and a PhD degree in physics from Cornell University. He did post-doctoral research at the University of Massachusetts and worked at Columbia University until 2003, when he took his present position at the University of New Mexico. His research primarily focuses on lipid layers and cell membranes, encompassing both fluorescence microscopy and ultrasound experiments and computer modeling of the membrane behavior.

Mei-Hwa Lee

Mei-Hwa Lee received his PhD degree from National Taiwan University in Taiwan in 2000, and was an associate researcher at Medical and Pharmaceutical Industry Technology and Development Center from 2001 to 2003. Then, she joined I-Shou University (Kaohsiung, Taiwan), and now she is a professor in the Department of Materials Science and Engineering. Her expertise is in the field of microemulsion formulation; ceramic materials and biosensors. She has published over 200 peer-reviewed papers.

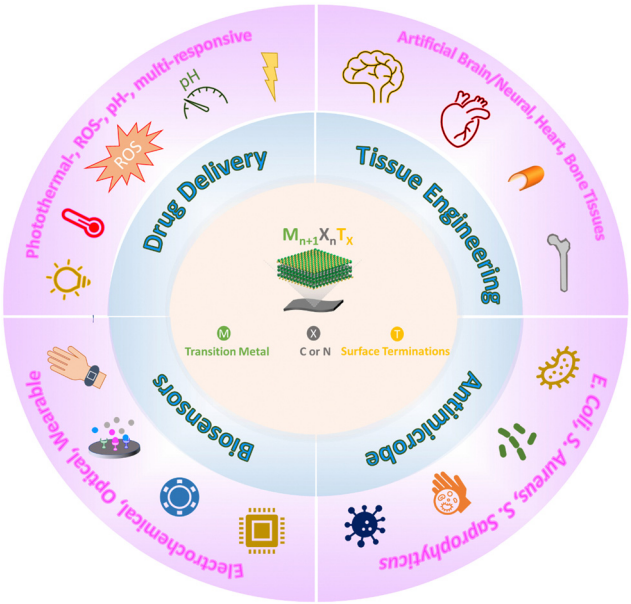

Fig. 1 The structure of this review, including the MXene structure, application of MXenes in drug delivery, applications of MXenes in tissue engineering, antimicrobial applications of MXene-based materials, and applications of MXenes in biosensors.

(layered transition metal carbides and carbonitrides) using hydrofluoric acid.[6] Processing techniques using supercritical fluids (SCFs) were then developed for enhancing exfoliation efficiency and product quality.[7] As shown in Fig. 2, multiple additional synthetic approaches have subsequently been developed, including selective etching in a mixture of fluoride salts and various acids, and the use of non-aqueous etchants, halogens, or molten salts. These new synthetic approaches have allowed the creation of new MXenes with better control over their surface chemistries.[6]

Hung-Yin Lin

Hung-Yin Lin received his PhD degree from Columbia University in the City of New York in 2003. He joined the National University of Kaohsiung (Taiwan) in 2005, and is currently a distinguished professor in the Department of Chemical and Materials Engineering. He has published over 300 peer-reviewed papers, and was elected as a fellow of the Royal Society of Chemistry (FRSC) and Royal Society of Biology (FRSB) in 2015 and 2023, respectively. His expertise is in the field of translational biomedical engineering, and he is now an Associate Editor of Frontiers in Bioengineering and Biotechnology.

2. MXenes and targeted delivery

2.1. Applications of MXenes in photothermal therapy and synergistic therapy

Photothermal therapy (PTT) is a promising approach for eradicating tumors by inducing localized hyperthermia, thereby minimizing adverse side effects. Photothermal agents generate localized heat upon exposure to light, leading to cancer cell destruction. The effectiveness of photothermal agents hinges on two factors: their light-absorption capability, determined by the extinction coefficient (ε), and their ability to generate heat when exposed to external light, known as photothermal conversion efficiency (PCE, η). Among various carbon-based 2D materials, 2D MXenes stand out due to their remarkably high PCE, attributed to their robust near-infrared (NIR) absorption and low radiative decay. This indicates their potential as highly efficient photothermal agents for cancer hyperthermia, utilizing external NIR laser irradiation.[8]

In general, 2D MXenes like titanium carbide (Ti_3C_2) and niobium carbide (Nb_2C) MXenes are employed for photo-triggered cancer hyperthermia due to their high photothermal conversion efficiency. However, despite their high PCE, Ti_3C_2 MXenes eliminate cancer cells with relatively low efficiency, possibly owing to insufficient biocompatibility and/or stability; thus, it is important to enhance these properties of Ti_3C_2 MXenes for achieving more effective cancer treatment. Lin *et al.* have made strides in enhancing biocompatibility and physiological stability through surface modification of 2D Ta_4C_3 MXene nanosheets with soybean phospholipids.[9] The 2D Ta_4C_3 MXene nanosheets demonstrate exceptional NIR photothermal capabilities with a reasonable extinction coefficient of 4.06 L g^{-1} cm^{-1} at 808 nm, an extraordinarily high photothermal conversion efficiency of 44.7%, and remarkable photothermal stability.[9] Han *et al.* harnessed the exceptional drug-loading capacity and photothermal conversion properties of Ti_3C_2 MXene, leveraging the synergistic effects of photothermal therapy and chemotherapy, as shown in Fig. 3(a) and (b).[10,11] Their investigations encompassed both *in vitro* and *in vivo* assessments of tumor clearance. As shown in Fig. 3(c), the *in vitro* photothermal conversion prowess of Ti_3C_2-SP was assessed by monitoring the temperature increase of an aqueous solution following exposure to 808 nm laser irradiation at a power density of 1.0 W cm^{-2}.[11] The temperature exhibited a progressive rise corresponding to increasing Ti_3C_2-SP concentrations (0, 38, 75, 150, and 300 μg mL^{-1}).[11] Following a 5-minute near-infrared (NIR) irradiation at 808 nm, the temperature reached 52 °C at a concentration of 300 μg mL^{-1}.[11] These MXenes exhibited an impressive drug-loading capacity, reaching up to 211.8 wt/wt% as shown in Fig. 3(d), and exhibited both pH-responsive and near-infrared laser-triggered drug release capabilities. Furthermore, these 2D MXenes could be used as contrast agents for photoacoustic imaging, offering theranostic potential, Fig. 3(e) and (f). Finally, their superior *in vivo* biocompatibility and efficient clearance from the body have been comprehensively evaluated, underscoring their robust biosafety profile and potential for clinical translation.[11]

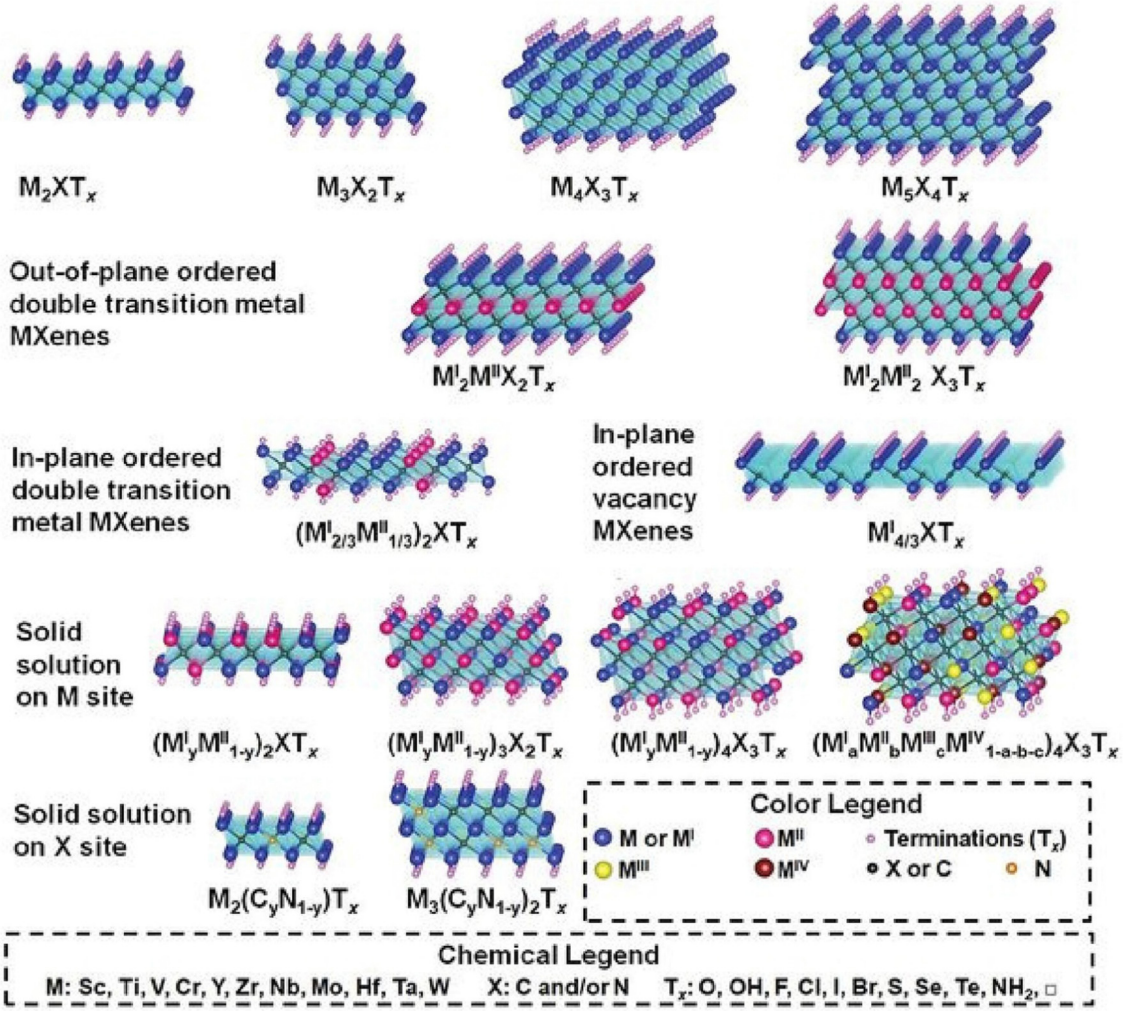

Fig. 2 MXenes have a formula of $M_{n+1}X_nT_x$, where M is an early transition metal, X is C or N, T_x represents surface terminations (the n value can vary from 1 to 4; the M sites can be occupied either by one, two, or more transition metal atoms, forming solid solutions or ordered structures).[6] The ordered double transition metal MXenes exist as in-plane ordered structures (i-MXenes), *e.g.*, $(Mo_{2/3}Y_{1/3})_2CT_x$, in-plane vacancy structures, *e.g.*, $Mo_{2/3}CT_x$, and out-of-plane ordered structures (o-MXenes) where one or two layers of MII transition metal are sandwiched between layers of MI transition metal, *e.g.*, $Cr_2TiC_2T_x$ or $Mo_2Ti_2C_3T_x$.[6] Reprinted with permission from Wiley, copyright 2021.[6]

MXene nanosheets in PTT have predominantly been employed within the first NIR-I biowindow (750–1000 nm); exploration of the second NIR-II biowindow (1000–1350 nm) has been limited. In contrast to the well-established NIR-I biowindow, operating within the NIR-II biowindow offers two distinct advantages: a greater maximum permissible exposure and an enhanced laser penetration depth. Lin *et al.* found that Nb_2C nanosheets exhibit remarkable NIR-I and NIR-II absorption, along with extraordinarily high photothermal conversion efficiency.[13] The 2D Nb_2C nanosheets were synthesized through a two-step liquid exfoliation process that involved sequential delamination and intercalation procedures. These Nb_2C nanosheets demonstrated remarkably high photothermal conversion efficiency, reaching 36.4% in the NIR-I spectral range and 45.6% in the NIR-II spectral range. Moreover, their photothermal performance remained stable over time. Following surface modification with polyvinylpyrrolidone (PVP), the resulting Nb_2C–PVP colloids exhibited outstanding biocompatibility and physiological stability, showing no discernible toxicity both *in vitro* and *in vivo*. Han *et al*. utilized versatile sol–gel chemistry to create a distinct ''therapeutic mesopore'' layer on the surface of 2D Nb_2C MXene.[14] This layer capitalizes on the characteristics of mesoporous structures to serve as a reservoir for loading and delivering therapeutic agents.[14] These developments open new avenues for MXene-based PTT in the NIR-II biowindow, capitalizing on its unique advantages.[13]

Using MXenes for simultaneous PTT and drug delivery has been explored by Zhu and colleagues.[12] Platinum (Pt) nanoparticles exhibit peroxidase-like (POD-like) activity, capable of generating hydroxyl radicals (•OH) that induce cell apoptosis and necrosis as shown in Fig. 3(g).[12] Such particles have been referred to as ''artificial nanozymes'' due to their catalytic activity. Zhu *et al.* prepared Ti_3C_2 nanosheets decorated with Pt-(poly(ethylene glycol), PEG) to leverage hyperthermia-enhanced nanozyme catalytic activity for cancer therapy.[12]

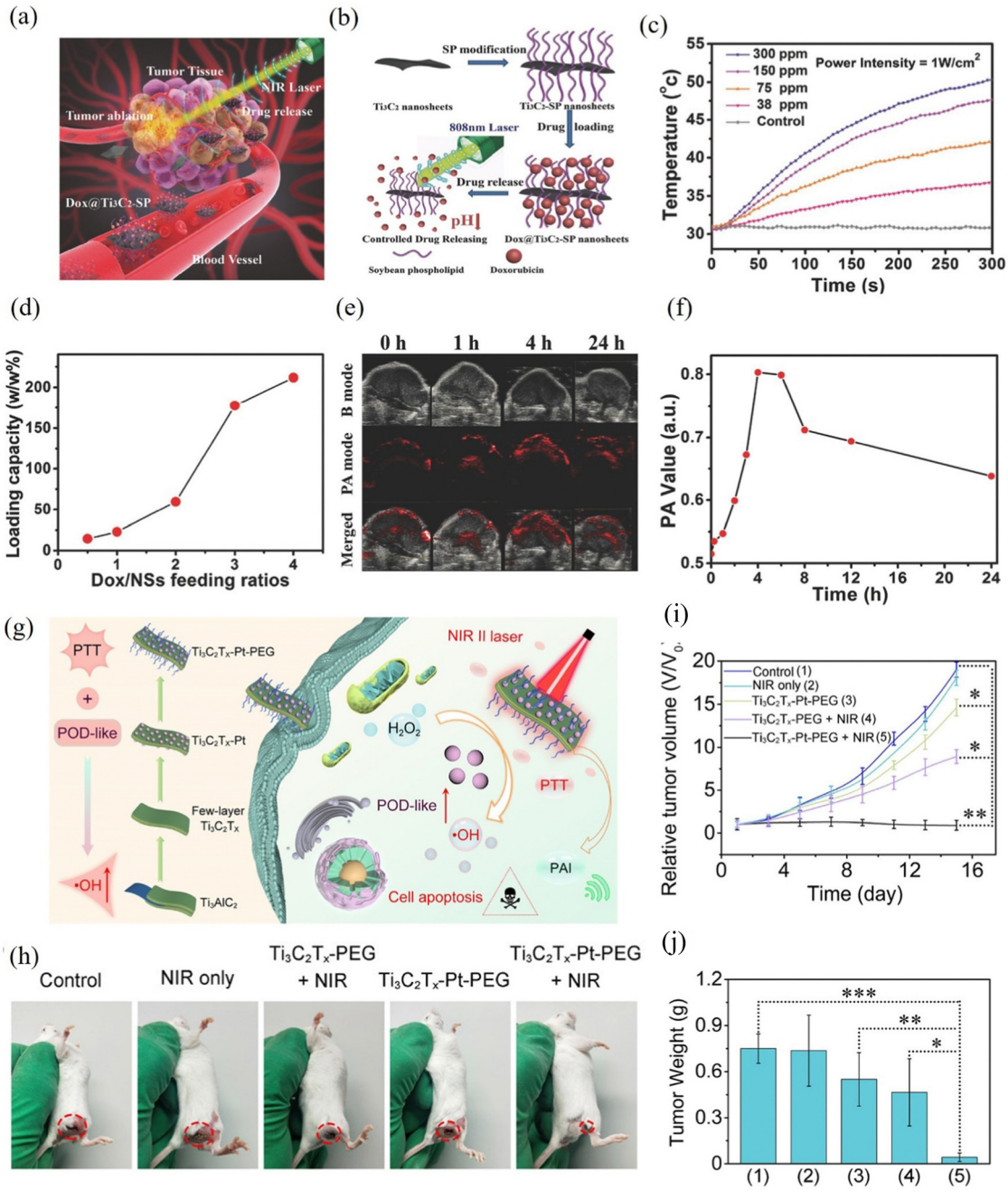

Fig. 3 The scheme of the synthetic process and functionality of MXene-SP for synergistic effects on cancer therapy. (a) A schematic illustration of the Ti_3C_2-based drug delivery system for *in vivo* synergistic photothermal and chemotherapy of cancer is presented. This includes the processes of transport within the blood vessel, accumulation within the tumor, controlled drug release, and NIR-triggered photothermal ablation of tumor tissue.[11] (b) The schematic representation outlines the surface modification of Ti_3C_2 nanosheets using SP, followed by their surface drug loading, and responsive drug release triggered either from within or through external irradiation.[11] (c) Photothermal heating curves of Ti_3C_2-SP nanosheets at varying concentrations when exposed to 808 nm laser irradiation (1.0 W cm^{-2}). Additionally, (d) the Dox-loading capacities of Ti_3C_2-SP nanosheets at different Dox/Ti_3C_2-SP nanosheets ratios are presented.[11] (e) *In vivo* 2D ultrasound imaging, PA imaging, and merged US and PA images of the tumor following intravenous administration of Ti_3C_2-SP *via* the tail vein at various time points (pre-injection, 1 hour, 4 hours, and 24 hours).[11] (f) The corresponding quantitative changes of PA signal intensity within the tumor.[11] Reprinted with permission from Wiley, copyright 2023.[11] (g) Illustration of the diagram depicting $Ti_3C_2T_x$-Pt-PEG with hyperthermia-enhanced nanozyme catalytic activity for cancer therapy.[12] (h) Photographic documentation of the representative murine subjects, captured 15 days post-varied treatments, with delineation of the tumor regions through circumscribing.[12] (i) Relative tumor volume curves of 4T1 tumor-bearing mice after different treatments.[12] (j) Tumor weight changes in 4T1 tumor-bearing mice after different treatments. (g)–(j) Reprinted with permission from American Chemical Society, copyright 2023.[12]

Fig. 3(h)–(J) demonstrates the synergistic therapeutic efficiency of $Ti_3C_2T_x$-Pt-PEG nanocomposites. It was found that nanocomposite particles exhibit anti-tumor activity both through their enzymatic action and a photothermal effect upon NIR-II light irradiation, even at low power density (0.75 W cm^{-2}).[12]

Another example of synergistic drug release and PTT was reported by Xu *et al.* They designed a dual-therapeutic conjugate, DOXjade, responsive to the acidic microenvironment of tumors. This conjugate incorporates the clinically approved iron chelator deferasirox and doxorubicin (DOX). When DOXjade is loaded onto ultrathin 2D Ti_3C_2 MXene nanosheets with PVP modification, it forms a construct referred to as Ti_3C_2-PVP@DOXjade. This construct enables the photo-activation of iron chelation and chemotherapeutic functions of DOXjade specifically at tumor sites. Additionally, it exhibits a robust photothermal effect with photothermal conversion efficiencies of up to 40%. This approach achieved a tumor pH-responsive antitumor effect encompassing iron chelation, photothermal therapy, and chemotherapy, validated through both *in vitro* and *in vivo* experiments.[15]

Another approach for controlled release was explored by Yang and co-workers, who mixed MXene with magnetic iron oxide nanoparticles (MNPs@MXene) and then encapsulated MNP@MXene in a poly(*N*-isopropyl acrylamide) (PNIPAM)/alginate hybrid hydrogel through dual internal covalent- and ionic-cross-linked bonding.[16] The hybrid system contributes a novel strategy for a drug carrier with photothermal- and magnetic-responsive abilities. This carrier demonstrated high effectiveness in photothermally triggered drug release. The mechanism is thought to involve the thermally-induced expulsion of water from the hydrogel, effectively pumping the drug out of the carrier upon illumination. The studies described above show some of the remarkable advances in photothermal therapy and photo-triggered drug release achieved using the unique capabilities of MXenes.

2.2. ROS-, pH-, electrical- and multi-responsive properties of MXene-based drug delivery systems

Environmentally-responsive 2D materials with a broad range of biomedical applications have been developed in previous studies.[17–21] For example, Shen and co-workers have shown that cobalt-molybdenum-based 2D layered double hydroxide (LDH) nanosheets (CoMo-LDH) can be used for photo-responsive dynamic therapy for cancer treatment. The CoMo-LDH nanosheets contain, by design, defects in the structure that enhance their photocatalytic and electrocatalytic activities. After treating with NIR-III 1567 nm, the nanosheets can catalyze the formation of H_2O_2, leading to tumor cell apoptosis.[22] In addition, Hu and co-workers have created cobalt-tungsten LDH (CoW-LDH) nanosheets with a small bandgap.[23] Electron–hole pairs can be excited and separated to generate $^1O_2$ and $^\bullet O_2^-$ in CoW-LDH nanosheets under ultrasound stimulation.[23] The reactive oxygen species (ROS) generated by this sonodynamic effect can induce cancer cell cell apoptosis.[23] In addition to the photothermal properties of MXene nanomaterials, scientists are also eager to apply the physiochemical properties (such as high surface area and reactivity) of MXene nanomaterials to develop versatile carriers with different responsive behaviors for new drug delivery systems. Zhang and co-workers developed an MXene nanocarrier with dual responsiveness (pH and reactive oxygen species, ROS) to control drug release behaviors.[24] First, the MXene surface was modified to an amine-rich interface and then doxorubicin was bound using 3,3′-diselenodiyldipropionic acid (DSeDPA) as a cross-linker. During the conjugation process, DSeDPA can first form an amide bond on the MXene surface, and then the remaining carboxylic acid groups on DSeDPA provide a site for conjugation with doxorubicin (DOX) molecules through an EDC/NHS reaction, resulting in the generation of MXene-Se-DOX. DOX was not released from MXene-Se-DOX under either weakly acidic or healthy physiological conditions (<3% in pH = 5.5 and pH = 7.4), preventing premature release and the associated ill side effects. However, the diselenide bond from 3,3′-diselenodiyldipropionic acid is easily broken by reducing agents, leading to a 20–30 times enhancement in DOX release when using hydrogen peroxide and glutathione as reducing agents. Many reports have demonstrated that ROS levels, including hydrogen peroxide, are higher in tumor tissues than in normal tissues.[25,26] In addition, previous studies have also reported that the rapid growth and metabolism of cancer cells contribute to an acidic environment and overexpression of glutathione in the tumor microenvironment.[27,28] At pH 5.5, glutathione-triggered DOX release was much greater than hydrogen peroxide-triggered release, while differences were smaller at pH 7.4. These results revealed that the MXene-Se-DOX nanocargo has a dual (ROS- and pH-) responsive function and has great potential as a responsive system for tumor therapy.[29]

3. Application of MXenes in tissue engineering

Recently, biomimetic environments with electrical stimuli have shown their importance in regulating various physiological bioactivities in embryogenesis, skeletal tissue movement, and tissue regeneration: electrical energy plays a crucial role in the human body and its development.[30,31] In contrast to other 2D materials, MXene exhibits superior biocompatibility and hydrophilicity. In comparison to graphene and reduced graphene oxide (rGO), the prominently negative zeta potential (ranging between −30 and −80 mV) endows MXenes with the capability to readily form stable colloidal dispersions without aggregation in diverse aqueous and organic solvents. In addition, its elevated specific surface area facilitates drug or growth factor loading, and it possesses antimicrobial properties conducive to biological implantation.[32] The initial variant of MXene discovered exhibits outstanding electrical conductivity and volumetric capacitance, measuring approximately 10 000 S cm^{-1} and 1500 F cm^{-3}, respectively. Notably, the volumetric capacitance of MXene surpasses that of graphene by several orders of magnitude (60–100 F cm^{-3}). These exceptional electrical

properties position MXene as a promising candidate for regenerating electrically active tissues, including cardiac and neural tissues.[33]

Owing to active functional groups and high hydrophilicity, MXenes are readily used to develop versatile functional complexes by integrating with other materials. Many studies have developed or synthesized new MXene-derived nanocomplexes to improve the poor electrical and mechanical properties of biopolymers or synthetic polymers. For example, Lin and coworkers generated a multifunctional wound dressing hydrogel by mixing bacterial cellulose and MXene. By adding MXene, the hydrogel achieved the desired mechanical properties and flexibility; Mxene conductivity contributed to an electrical stimulation effect for wounds, and provided better healing behaviors compared to commercial Tegaderm films.[34] The electrical/conductive properties of MXenes may be useful in almost any tissue engineering or regeneration application. In this review, we focus on neural, cardiac, and bone tissue engineering applications. Finally, in contrast to other 2D materials, mono- or few-layer MXene flakes exhibit instability in environments containing oxygen and water, a characteristic that may enhance their biodegradability.[32] Lin *et al.* investigated the biodegradability of Nb_2C–PVP nanosheets (NSs) in human myeloperoxidase (hMPO). Dynamic light scattering (DLS) measurements of Nb_2C NSs treated with hMPO revealed multiple peaks corresponding to size reduction, compared to untreated controls. Additionally, visible-near-infrared (vis-NIR) absorbance spectra of treated nanosheets demonstrated a significant size decrease during biodegradation. Profound alterations in nanosheet morphology were further affirmed through transmission electron microscopy (TEM) images. Consequently, the authors assert that a route of enzyme-triggered biodegradation of Nb_2C NSs has been achieved, enabling their harmless degradation under simulated conditions within a reasonable in-body period after fulfilling their therapeutic functions.[13]

3.1. Mxene-based materials for neural tissue engineering

Injuries afflicting the peripheral (PNS) and central (CNS) nervous systems have the potential to cause the loss of motor and sensory faculties, exerting a substantial impact on the overall quality of life in affected patients. The PNS and CNS demonstrate inadequacy in their regenerative capacities subsequent to such injuries; thus, the development of methods that allow neural cell regrowth is imperative. Conventional therapeutic approaches, such as autografts, allografts, and pharmaceutical agents, have limitations and are often insufficient to fully restore nervous system injuries. Neural tissue engineering, *i.e.*, utilizing biomaterials to guide nerve cell interactions, steer their growth, enhancement, proliferation, and specialization, holds much promise. During the maturation of the nervous system, electrical activity assumes a prominent role in governing signal transmission and the functioning of neuronal networks. Thus, electrical nanomaterials and tissue engineering have gained considerable recognition as potential solutions for effective tissue regeneration.

Among the various materials being explored, 2D nanomaterials have emerged as a central focus in tissue engineering and regenerative medicine.[35] These nanomaterials possess exceptional physicochemical and biological properties, making them highly valuable for these applications. Given their exceptional electrical conductivity, mechanical adaptability, and inherent hydrophilicity,[36] the notable conductivity of MXenes makes them particularly promising candidates for developing innovative scaffolds in neural tissue engineering.[37] This conductive property can potentially aid in the development of substrates that more closely mimic the natural electrical environment of neural tissues, thus promoting cellular growth, differentiation, and overall tissue integration.[38] Furthermore, the high loading capacity of MXene nanomaterials has captured the interest of researchers for their potential use in drug and gene delivery for treating various severe nervous system disorders. Their ability to efficiently encapsulate therapeutic agents and deliver them to specific sites within the nervous system holds great potential for targeted and effective treatments. The exploration of MXene's application in nerve regeneration encompasses the utilization of 2D substrates infused with MXenes, the integration of MXene nanosheets within three dimensional (3D) hydrogels, and 3D bioprinted or electrospun matrices.[39] However, in this relatively new field, there is still limited literature on the application of MXene in neural tissue engineering, with most studies focusing on *in vitro* experimental designs at present.

The biocompatibility and the nanotoxicology of MXenes have been documented across various neural cell types. Wu and colleagues previously assessed the biotoxicity of Ti_3C_2 on primary neural stem cells (NSCs) and differentiated cells derived from these stem cells.[40] This evaluation encompassed various facets, including apoptosis, cellular viability, uptake, maintenance of cell membrane integrity, and an analysis of global gene expression profiles. Their investigation revealed that Ti_3C_2 exerted dose-dependent cytotoxic effects on both NSCs and differentiated cells derived from NSCs. Remarkably, at a concentration of 12.5 μg mL^{-1}, Ti_3C_2 nanosheets exhibited no discernible adverse impact, but at a concentration of 25 μg mL^{-1}, they induced notable apoptosis and disrupted the integrity of the cell membrane. Furthermore, the study showed that NSCs took up small quantities of Ti_3C_2 MXene nanosheets, with the majority of these nanosheets residing outside the NSCs. Exposure to Ti_3C_2 MXene nanosheets triggered an inflammatory, defensive, stress-related, and stimulus response within the NSCs. These studies indicate that the safety impact of MXene concentration on normal cells remains non-negligible. Mitigating the cytotoxicity of MXene through surface modification and property adjustments will be a crucial consideration for its application in tissue engineering.

Guo and colleagues distributed Ti_3C_2 MXene onto tissue culture polystyrene. Following this, they cultivated neural stem cells (NSCs) on the MXene coated with laminin, with the intent of probing its impact on the regulation of cellular survival and behavior. Notably, their findings indicated that these cells thrived on both $Ti_3C_2T_x$ MXene and tissue culture polystyrene

(TCPS) substrates, displaying steadfast adhesion and further exhibiting substantial expansion of their terminal extensions.[41] Driscoll *et al.* conducted cytotoxicity studies *in vitro* using primary cortical neurons cultivated on Ti_3C_2 MXene films. The quantification of viable neurons revealed no notable disparity in cell survival when compared to control polystyrene cultures. However, after 7 days of culture, they found that cells on Ti_3C_2 MXene were notably more sparse, in comparison to those grown on polystyrene. This implies that additional surface treatments may be necessary for facilitating neuronal adhesion and growth. While there was a reduction in overall neurite density in the Ti_3C_2 MXene cultures, no significant differences were observed in neurite outgrowth per neuron.[42] The aforementioned studies collectively demonstrate that MXenes exhibit dose-dependent biocompatibility (*i.e.*, compatible at low doses) and possess the capacity to support neuron growth and the establishment of neural networks.

As shown in Fig. 4, Zhang *et al.* developed a composite hydrogel by combining Ti_3C_2 MXene with Matrigel and explored its impact on the pluripotency of cochlear organoids,

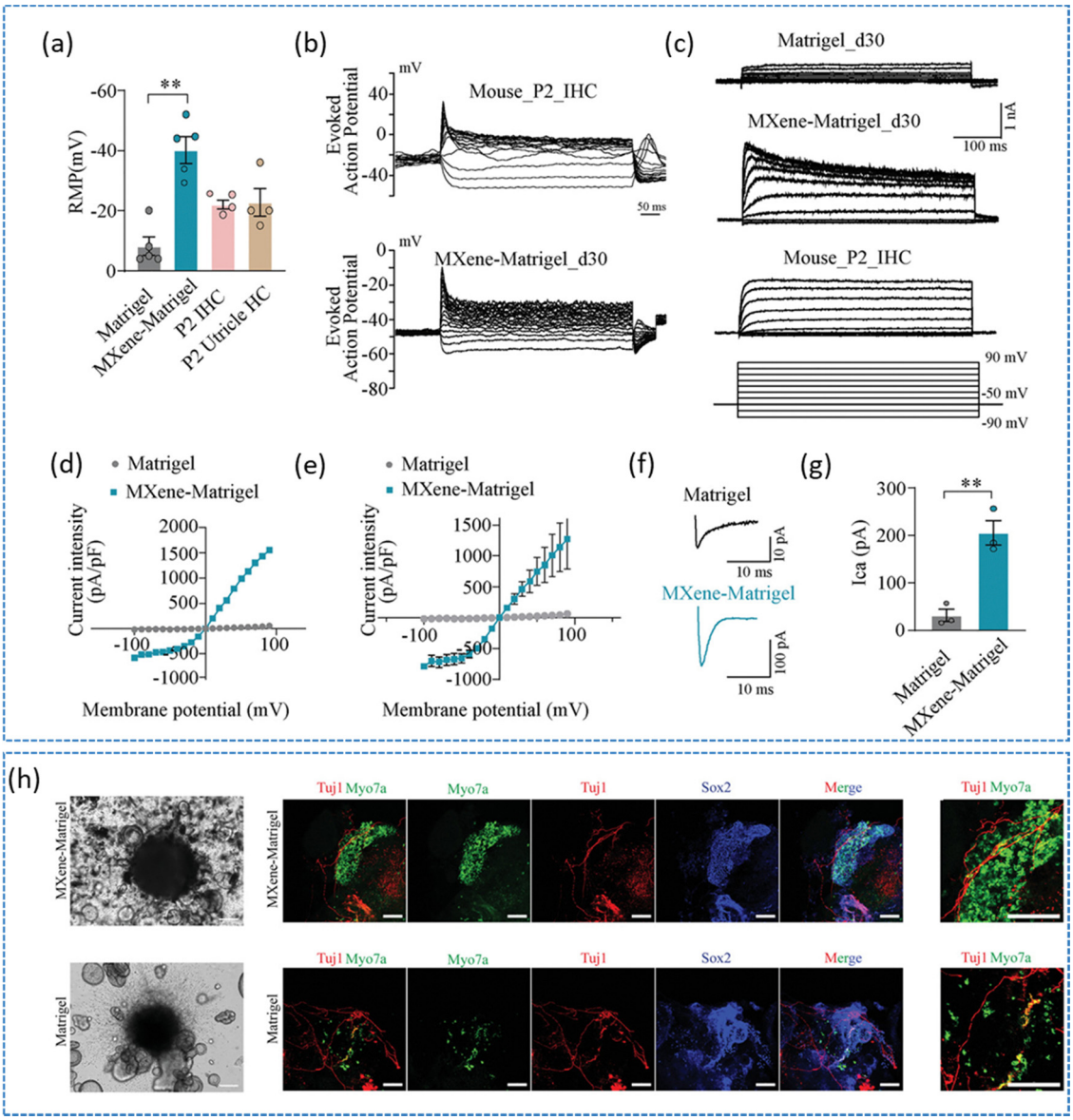

Fig. 4 Functional organoid hair cells in MXene-Matrigel exhibited better electrophysiological properties.[45] (a) Statistic results of RMP of regenerated organoid hair cells in the Matrigel and MXene-Matrigel substrates after differentiation for 20 days (d30), P2 native IHCs, and P2 utricle hair cells.[45] (b) Representative evoked spikes recorded under current-clamp, from native (WT) IHCs at P2 and organoid hair cells (d30). (c) Representative K^+ currents recorded. (d) and (e) The *I*–*V* plot of the averaged fast component (d) and low component (e) of the K^+ currents.[45] (f) Representative calcium currents (Ica) recorded in response to a voltage ramp from −87 to +63 mV in 150 ms under voltage clamp, from organoids hair cells of the Matrigel group or the MXene-Matrigel group at d30. (g) Statistic results of the peaks of Ica, recorded from organoid hair cells of the Matrigel group or the MXene-Matrigel group at d30. (h) Cochlea-Orgs co-cultured with modiolus and form synapse-like contacts with sensory neurons.[45] Reprinted with permission from Wiley, copyright 2023.[45]

particularly in enhancing the development and maturation of hair cells within these organoids.[33] Fig. 4(a)–(g) show that functional organoid hair cells in MXene-Matrigel exhibited better electrophysiological properties than those grown on TCPS.[33] Their research revealed that MXene-Matrigel facilitated the establishment of connections between regenerated hair cells and spiral ganglion neurons (SGNs), as shown in Fig. 4(h), which grew from the cochlea modiolus in a co-culture system.[33] Additionally, MXene-Matrigel enhanced the efficiency of synapse formation.[43] Liao *et al.* have introduced an electrical stimulation system created through the integration of a cochlear implant with a conductive hydrogel composed of Ti_3C_2 MXene and Matrigel. This 3D Ti_3C_2 MXene hydrogel was found to have a beneficial effect on the growth and maturation of SGNs.[44]

MXene-infused hydrogels have also been explored as neural growth guides. Cai *et al.* designed a nerve conduit utilizing a gelatin methacryloyl (GelMA)-MXene hydrogel, which incorporated both conductive properties and a microgroove structure. This innovative approach aimed to enhance the microenvironment at the site of spinal cord injury and facilitate the connection between newly generated nerves and the injured neurites. *In vitro* experiments conclusively demonstrated that the grooved GelMA-MXene hydrogel significantly enhanced the adhesion, proliferation, and differentiation of NSCs. Additionally, through animal experiments, the viability of the scaffolds for spinal cord injury was explicitly established *in vivo*.[46]

In contrast to flat surfaces, substrates composed of highly oriented fibers demonstrate a superior ability to stimulate crucial neuronal differentiation, facilitate cell migration, and encourage neurite extension. This phenomenon is primarily attributed to the influence of contact guidance.[47] Electrospinning is a versatile technique employed for fabricating polymeric fibrous scaffolds, with fibers ranging in diameter from micrometers to nanometers. These fibrous scaffolds closely resemble the native extracellular matrix. Various natural and synthetic polymers, including polycaprolactone (PCL), poly(lactic acid) (PLA), poly(glycolic acid) (PGA), cellulose, chitosan, and gelatin (among others), are extensively utilized for fiber production in this process. In one study, poly-L-lactic acid (PLLA) nanofibers were produced through electrospinning, creating an extracellular scaffold comprising aligned PLLA nanofibers with an additional $Ti_3C_2T_x$ MXene coating layer.[48] These conductive scaffolds play a pivotal role in orchestrating intercellular communication among NSC-derived neurons by facilitating the formation of functional electrical synapses. This, in turn, fosters neuronal maturation and amplifies the beneficial effects of applied electrical stimulation, ultimately enhancing the regeneration of nerve tissue. Notably, the MXene coated, aligned PLLA nanofiber scaffold exhibits significant advantages for *in vivo* applications, particularly in terms of mitigating the host immune response and reducing tissue fibrosis. Electrospinning (and spray coated) was also used by Nan *et al.* to fabricate nerve guidance conduits (NGCs) composed of MXene-PCL. The impact on nerve regeneration was assessed both *in vitro* and *in vivo*. Remarkably, MXene-PCL NGCs demonstrated comparable outcomes to autografts in terms of the sciatic function index, electrophysiological examination, angiogenesis, and morphological nerve regeneration. These findings suggest that the conductive MXene-PCL NGC has the potential to transmit physiological neural electric signals, stimulate angiogenesis, and promote nerve regeneration.[49]

Electrical stimulation (ES) has been employed within cell culture systems to augment various aspects of NSC behavior, including proliferation, neuronal differentiation, and migration. Also, efficient ES can serve as a promising method for modulating the behavior of excitatory cells, particularly to enhance nerve regeneration and to accelerate peripheral nerve cell growth. ES has been used with a number of MXene-containing scaffolds or substrates. Guo *et al.* have cultured primary NSCs on a laminin-coated MXene film, and the combination of electrical stimulation and MXene films substantially augmented the proliferation of NSCs. Li *et al.* conducted a study in which they cultured NSCs on MXene substrates to investigate the impact of this substrate on the morphological and electrophysiological characteristics of neurons derived from NSCs. Previous studies have revealed that the combination of ES with MXene not only supported the regular growth of NSCs but also significantly boosted NSC proliferation. Moreover, this enhanced proliferation coincided with increased efficiency in neuronal differentiation, suggesting that MXenes can facilitate the maturation of NSCs.[38,50] Li *et al.* also demonstrated that MXene facilitated the differentiation of NSCs and promoted neurite growth. Furthermore, MXene increased the voltage-gated Ca^{2+} current in mature neurons, although it had no significant effect on Na^+ or K^+ currents. This resulted in heightened neuronal spiking activity without altering passive membrane properties, and also enhanced synaptic transmission among the neurons.[50] Xiao *et al.* conducted experiments to comprehensively investigate the impact of MXene interfaces on the biophysiological characteristics of targeted neurons and *in vitro* neuronal circuits, particularly the influence of uncoated MXene interfaces on neuronal electrophysiological behavior. Calcium imaging, and the measurement of spontaneous and miniature postsynaptic currents were employed to demonstrate that MXene interfaces preserved the fundamental physiology of neural microcircuits.[51] Qi *et al*. developed a wireless magnet-powered electrical stimulation system induced by a rotating magnetic field using conductive MXene-coated PLLA particles. They showed an excellent conductivity of 8.44 S m^{-1} and generated a current of 10 μA. *In vitro* testing revealed enhanced PC12 cell proliferation, neurite growth, and differentiation into mature neurons.[52] In a study on cochlear implants discussed above, Liao *et al.* developed an electroacoustic stimulation system for cochlear implants, utilizing a conductive MXene–matrigel hydrogel, to investigate the behavior of SGNs. They found that low-frequency stimulation played a crucial role in promoting growth cone development, neurite outgrowth in SGNs, and facilitating signal transmission between these cells. This research holds potential for the clinical application of MXene hydrogel to enhance the postoperative auditory outcomes of cochlear implantation, thereby benefiting individuals

with sensorineural hearing loss.[44] Notably, in addition to utilizing MXene's conductivity for neural induction, Wang *et al.* have shown that 2D MXenes can be harnessed for remote and photothermal stimulation of neuronal electrical activity at subcellular precision. Their research revealed that MXene requires similar incident energy densities to stimulate neurons compared to a photoelectrically active p–i–n Si membrane and Si nanowires.[53]

3.2. Mxene-based materials for cardiac tissue engineering

Cardiovascular diseases are irreversible and often lead to patient disability or death. Annually, over 18 million deaths globally are attributed to cardiovascular diseases.[54] Among these, myocardial infarction stands out as a common yet often not easily detected cardiovascular ailment resulting from decreased or obstructed blood flow. This condition leads to prolonged inadequate oxygen supply, hemodynamic deterioration, and irreversible necrosis of the cardiac muscle. Consequently, cardiac tissue injury arising from myocardial infarction or coronary artery disease stands as a leading cause of morbidity and mortality worldwide.[55] This damage is permanent due to the cardiac tissue's limited regenerative capacity. The current long-term strategies for managing cardiac injuries involve pharmacological interventions and heart transplantation.[56] In the past decade, promising new approaches in regenerative medicine and tissue engineering have been explored– approaches that may eventually benefit millions of people.[57] Normal cardiac tissues possess specific contractile properties that are directly related to cellular orientation and elongation. Therefore, to replicate the properties of cardiac tissues *in vitro*, it is critical to engineer cardiac tissue with controllable mechanical properties to mimic the *in vivo* anisotropic structure of the myocardium encompassing its biophysical and topographical features. Based on these requirements, engineered cardiac tissues generally involve scaffolds made up of biodegradable and biocompatible materials, cellular components such as stem cells, and growth factors, and can reconstruct the structure and function of native cardiac tissues across different scales.[58] Additionally, cardiac muscles are electrically conductive ($\sim$0.1 S m^{-1}) and contain nanofibrous architectures with diameters ranging from 10 to 100 nm.[59] Therefore, the incorporation of nanomaterials with electrical conductivity into engineered cardiac tissues plays a vital role in endowing engineered cardiac tissues with appropriate electrical properties.

In the past five years, conductive material-hybrid scaffolds have been widely used in cardiac tissue engineering applications.[60] For example, gold nanorods/nanoparticles,[61] graphene, graphene oxide,[62] and carbon nanotubes[63] have been blended with conventional biomaterials, such as cryogels or hydrogels, to improve their electrophysiological properties. However, gold-, graphene-/graphene oxide-, and carbon nanotube-hybrid materials have a dose cytotoxicity issue, which limits the usage of these materials in clinical applications.[64–66] Compared with these conventional conductive materials, composites of MXene (carbonitrides, nitrides, and transition metal–carbon) provide a water-soluble system, large specific surface area, high cytocompatibility (compared with conventional conductive materials), and high electroconductivity.[9,67] These properties make MXene-based materials suitable candidates for clinical biomedical (and biosensing, see below) applications.[68] Ye and co-workers have developed mussel-like MXene-based cyrogels as a cardiac patch for cardiac tissue engineering (Fig. 5).[69] They mixed 0.8% MXene with PEG, GelMA, and dopamine-*N*′,*N*′-methylene-bisacrylamide to obtain a prepolymer solution; the MXene-hybrid prepolymer solution was placed in a −20 °C freezer overnight for cryogelation. Afterward, the cardiomyocytes isolated from 1–3 day old neonatal SD rats were cultured in MXene-hybrid cryogels. After 7 days of incubation, cardiomyocytes (CM) expressed mature cardiac-specific proteins, such as CX-43 and α-actin protein, and exhibited calcium transients and synchronous beating behavior. After transplanting the CM-laden MXene-cryogel patch into rats with myocardial infarction, they observed a reduction in inflammatory response, an acceleration of myocardial infarction recovery, and improved cardiac function.[69] Basara and co-workers developed MXene-based cardiac patches by using an aerosol jet printing technology. Briefly, they fabricated a PEG membrane as a base layer and then printed MXene onto the PEG layer. The MXene-PEG printed composite had a conductivity of 1.1 × 10^4 S m^{-1}, which is more than 100 000 times that of the pure PEG substrate (0.1 S m^{-1}). Through this technology, the induced pluripotent stem cell (iPSC)-derived cardiomyocytes could be aligned on the printed patterns, and this enhanced the expression of CM-43 protein and increased the calcium flux intensity and the synchronous beating area of mature cardiomyocytes from iPSCs.[70] These studies, although preliminary, suggest the possibilities for MXenes in cardiac tissue engineering.

3.3. Mxene-based materials for bone tissue engineering

Regeneration of large bone defects is a vital issue attracting scientists aiming to reconstruct the damaged bone after skeletal trauma, degenerative/cancer diseases, or bone fractures in the elderly population.[67] In general, the healing of large bone defects in the orthopedic regeneration field also poses a formidable issue because the critical-sized defects caused by tumor resection or skeletal trauma inhibit the spontaneous healing capacity of bone. Currently, various strategies are widely used to reconstruct bone defects in bone tissue engineering. For example, bone transplantation with autologous or allogeneic bone tissues presents a gold standard for reconstructing bones in clinical practice.[71] However, bone transplantation has limitations, including tissue resources, immunoreaction risk, and costly sample pre-treatment processes. Synthetic artificial substitutes combining cells, scaffolds, and chemical/physical stimuli may soon provide clinically effective solutions.[72,73]

Electrical currents and/or fields are an indispensable signal transduction factor that can activate some signaling pathways, such as the calcium–calmodulin pathway, and then upregulate growth factors or cytokines to accelerate osteogenesis.[74,75]

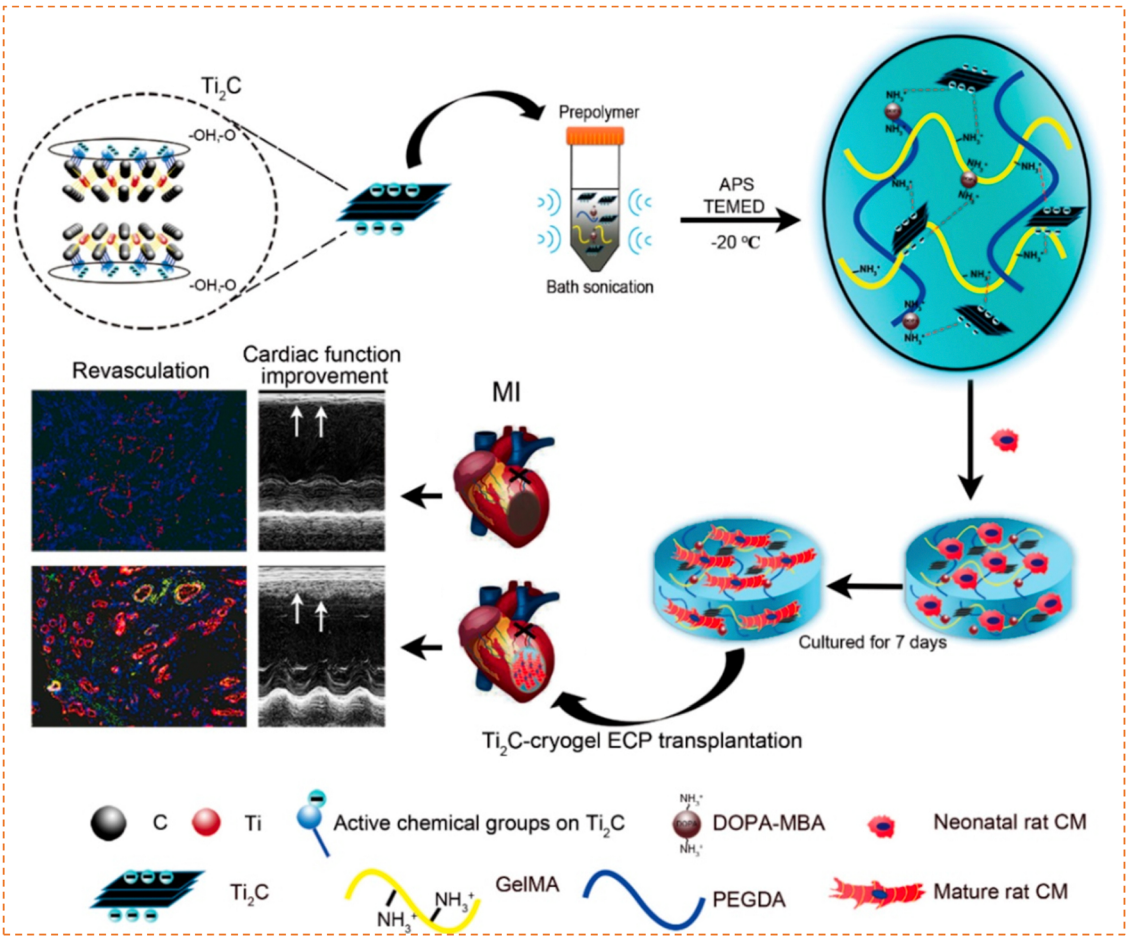

Fig. 5 The schematic image shows the fabrication of Ti_2C MXene nanoparticle-encapsulated-GelMA/(poly(ethylene glycol) diacrylate, PEGDA) hybrid cryogel. The HF-etched Ti_2C MXene nanoparticles were mixed with a GelMA/PEGDA prepolymer solution and formed a cryogel through a chemical cross-linking process at −20 °C. Afterward, the neonatal rat cardiomyocytes (CM) were cultured on the cryogel and matured after 7 days of incubation. Furthermore, the CM-laden engineering cardiac patch (EPC) contributes to revaculation and cardiac function improvement behaviors to the heart after transplantation into a rat myocardial infarction model. Reprinted with permission from Ivyspring International Publisher, copyright 2020.[69]

Therefore, the combination of artificial bone substitutes and electrical stimulation as a tissue engineering strategy is emerging as a popular adjunctive method to promote bone regeneration. For example, Yao and co-workers integrated a tricalcium phosphate-based gelatin scaffold with electroacupuncture technology to impart dual effects of biomaterials and electrical stimulation in rats with large bone defects. The study confirmed that electrical stimulation can promote the secretion of parathyroid hormone and calcium and then activate the osteoblast–osteoclast interaction to accelerate bone remodeling of large bone defects within 12 weeks.[76]

Currently, the osteogenic activity and new bone induction capacity of 2D nanomaterials such as MXene in bone tissue engineering are only beginning to be explored. Zhang and co-workers evaluated the osteoinductivity and new bone remodeling by MXene both *in vitro* and *in vivo*.[77] *In vitro*, MXene-coated substrates induced preosteoblasts with significant osteogenesis-related protein expressions (alkaline phosphatase(ALP), osteocalcin(OCN), and osteopontin(OPN)) in the osteogenic medium. The possible mechanism is that the MXene surface, rich in hydroxy groups, offers strong hydrogen bonding with proteins in the medium and then forms an osteoblast-like surface to induce cell adhesion and differentiation. Afterward, *in vivo* rat calvarial defect regeneration results showed that the MXene films promote early osteogenesis, rapid mineralization, with no inflammatory reactions. The MXene films enabled accelerated bone regeneration, compared to a titanium membrane, after 8 weeks. However, MXene films without cross-linking may be easily redispersed in the presence of a body fluid environment and then lose their mechanical strength and osteoinductive capability.[77] Recently, Hu and co-workers addressed this by developing a regenerated silk fibrin (RSF)-encapsulated MXene composite by using horseradish peroxidase (HRP) and hydrogen peroxide (H_2O_2) as a cross-linking strategy to form an internal dual-crosslinked network.[78] In their design, the RSF assembled on the MXene surface, and then the complex functional groups on MXene maintained the RSF fibril structure and further accelerated the formation of the β-sheet structure of RSF. Furthermore, the RSF-encapsulated MXene composite promoted conductivity and exhibited good

biocompatibility, which increased the wound healing effect in the presence of electrical stimulation. Furthermore, in their *in vivo* bone regeneration study, Hu and co-workers also confirmed that the MXene-based composite with electrical stimulation could enhance M2-type macrophage polarization to reduce inflammation and then activate the calcium-signaling pathway, promoting bone extracellular protein secretion, osteogenic differentiation of bone marrow stromal cells (BMSCs), mineralization, bone remodeling, and angiogenesis in a critical-size calvarial bone defect model after 12 weeks. The studies reviewed here show that MXene holds promise in playing an increasingly significant role in modifying scaffold/hydrogel properties, especially conductivity, for establishing an electrical environment in bone remodeling applications in bone tissue engineering.

4. Antimicrobial applications of MXene-based materials

Microbial infection is a concern in all tissue engineering and regeneration applications. There are three main areas of concern: (1) during tissue reconstruction or regeneration, biomaterials or engineered implants are usually prepared *in vitro* before transplantation and replacement of the damaged tissues through surgical procedures. Therefore, preventing microbial contamination ensures the preservation of the activity and functions of biomaterials and engineered implants. (2) Immune response/patient safety: wound contamination with microbes can cause a series of immune responses, resulting in tissue inflammation and the rejection of artificial implants by body tissues. (3) Biocompatibility and enhancement of success rates: the contamination of biomaterials or engineered implants by microbes creates a risk of degradation. Thus, it is desirable to engineer implantable materials with built-in antimicrobial activity. For example, Samie and co-workers developed an antibiotic-loaded silk fibroin-based electrospun composite with a controllable release profile, which significantly inhibits the growth of Gram positive and Gram-negative bacteria.[79]

In recent years, nanomaterials have confirmed their antimicrobial ability in many studies. For example, Zhao *et al.* developed silver nanoparticle-laden metal–organic framework (MOF) nanosheets for antimicrobial application.[80] They confirmed that MOF nanosheets can convert NIR energy to heat, which then accelerates the oxidation of Ag nanoparticles. Subsequently, the Ag ion can be released from the MOF nanosheets to kill microbes. Additionally, another group confirmed that molybdenum trioxide (MoO_3) nanomaterials have a photodynamic effect which can be used for antimicrobial applications.[81] They co-intercalated H_2O and Na^+ into the nanobelt of MoO_3 nanomaterials to shorten the length of the nanobelt. This change in the MoO_3 structure enhanced the absorption of NIR and generated more superoxide radicals targeting *Escherichia coli* and Saccharomyces aureus. The results yielded good antimicrobial effects in clinical periodontitis applications. These results encouraged further exploration of the potential antimicrobial functions of versatile 2D nanomaterials (such as Mo-base nanomaterials, graphene oxide/reduced graphene oxide, *etc.*).[82,83] For example, Xue and co-workers observed a size effect on photocatalytic activity in nanomaterials.[84] In their study, they showed that nanosheets with smaller sizes contributed to a higher photocatalytic ability to generate ROS than bulk nanomaterials and exhibited a higher antimicrobial activity for wound healing. Similarly, in Zn–Ti layered double hydroxide (LDH) nanosheets, there is a size effect on antimicrobial activity. Nanosheets with a controlled, small lateral size ($\sim$9 nm) provide a larger surface area and higher surface activity than large ($\sim$1 μm) particles. In small particles, titanium facilitates ROS generation under visible light. Small LDH nanosheets have thus been used as an antibiotic substrate, exerting a strong inhibition effect on the growth of *S. cerevisiae*, *S. aureus*, or *Escherichia coli*.[85] Yang and co-workers reported that MoS_2 obtained from a chemical exfoliation procedure provides an oxidation stress effect, which can cause damage to microbes and thus achieve antimicrobial activity.[82] In addition to their chemical activities, 2D nanomaterials may also co-inhibit microbial growth through their physical morphology, called the ''nano-knife'' effect. This is attributed to nanomaterials making direct contact with microbes and further offering a physical interaction that results in the disruption of their membrane.[86]

Zhu and co-workers developed a hybrid MXene nanomaterial with highly efficient and long-term antimicrobial activity by doping silver into $Ti_3C_2T_x$.[87] Ag-doped MXene nanomaterials were found to kill antibiotic-resistant microbes through a synergistic effect (photothermal properties and electrostatic attraction with the microbial cellular wall/membrane) upon exposure to NIR radiation. Furthermore, doped nanomaterial-encapsulated hydrogels have demonstrated their synergistic antimicrobial effects on infection inhibition in wound dressing applications in a mouse wound model and have enhanced wound healing under NIR radiation exposure.[87]

Photocatalytic activity can result from the electronic properties of MXenes[88] The multilayered structure contributes to a distinct intermediate energy level in MXene nanomaterials, which helps in electron–hole separation and enhances their photocatalytic performance.[89] Furthermore, under illumination, the nanohybrid structure enhances the photocatalytic effect, generating free radicals and inducing oxidative stress in microbes. For example, Li and co-workers designed Bi_2S_3/MXene nanomaterials based on an interfacial Schottky junction (Fig. 6).[90] The Schottky barrier in the Bi_2S_3/MXene structure inhibits electron backflow, promoting the transfer and separation of charges, which intensively enhances the generation of reactive oxygen species, killing over 99.8% *Escherichia coli and S. aureus* under NIR exposure within 10 minutes.[90]

The third antimicrobial mechanism of MXene nanomaterials is the physical inactivation/mechanical destruction. Through the direct contact between MXene nanomaterials and microbes, the sharp edges in the MXene layered nanostructure penetrate and destroy the microbial cell membrane, causing microbial damage and eventual death.[91] Using scanning electron microscopy (SEM) and atomic force microscopy

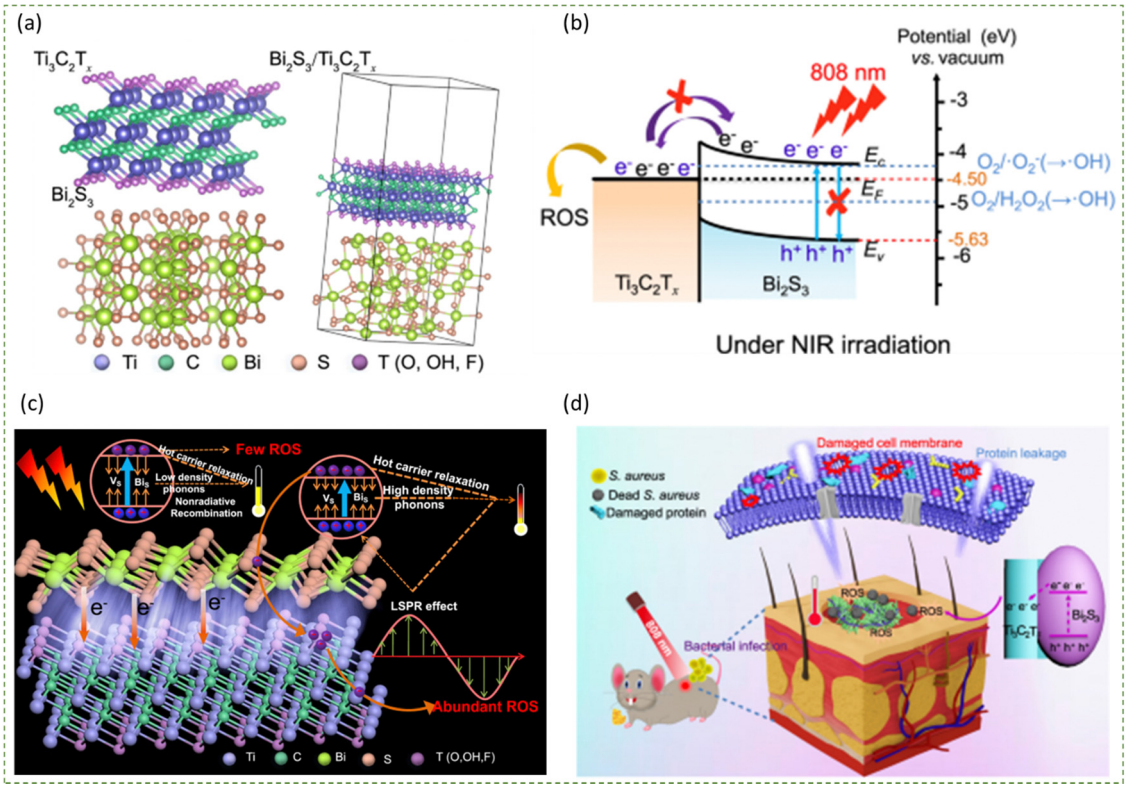

Fig. 6 (a) The optimization of the $Ti_3C_2T_x/Bi_2S_3$ hybrid complex. (b)–(d) Pure $Ti_3C_2T_x$ provides a low photothermal property owing to its LSPR effect, and Bi_2S_3 only generates inferior heat and few ROS under NIR irradiation. After combining $Ti_3C_2T_x$ and Bi_2S_3, Bi_2S_3 plays a role in facilitating the migration of photogenerated electrons into $Ti_3C_2T_x$ structures. It offers a Schottky barrier to prevent electronic backflow, increase the electron–hole pairs and photogenerated charges, and further enhance the ROS generation after NIR stimulation. Therefore, this $Ti_3C_2T_x/Bi_2S_3$ hybrid Schottky catalyst improves the photothermal function of $Ti_3C_2T_x$ MXene, resulting in an ROX effect that inhibits microbial activity. Reprinted with permission from Springer Nature Limited, copyright 2020.[90]

(AFM) imaging, Rasool and co-workers found that MXenes significantly damage the microbial membrane through direct physical contact.[92] Additional evidence for a direct physical interaction is obtained from growth curves of *E. coli* and *B. subtilis* in the presence of MXene nanosheets of different (lateral) sizes (0.09, 0.35, 0.57 and 4.40 μm). The smaller MXene nanosheets provide more sharp edges (per unit mass) and cause significant damage to microbial membranes and antimicrobial activity within 3 hours.[93] Similarly, Pandey and co-workers synthesized two different MXenes (Nb_2CT_x and $Nb_4C_3T_x$) to investigate the effects of the size and atomic structure of MXene on antimicrobial activity.[94] They found that the activity of microbes (*E. coli* and *S. aureus*) progressively decreases as the lateral size of Nb_2CT_x and $Nb_4C_3T_x$ nanosheets is reduced. These studies all suggest that the lateral sheet size and atomic structure of MXene nanosheets play an essential role in regulating and optimizing the antimicrobial ability of MXene nanomaterials.

5. The applications of MXenes in biosensors

MXenes with outstanding optical, electrical, thermal, and mechanical properties have been developed as sensing elements for use in physical, chemical, and biological sensing fields.[95] Compared with other 2D materials, MXenes are easily functionalized with groups (such as O, F, and OH) on their surfaces, which can then be conjugated with more biocompatible materials or receptors for specific sensing. In addition, the multiple layer structure of MXene provides higher conductivity compared to other (typically single layer) 2D materials.[96] Recently, Tran *et al.* examined the structures of MXenes, discussed various synthesis procedures, and analyzed physicochemical properties, particularly optical, electronic, structural, and mechanical properties for electrochemical sensors, gas sensors, biosensors, optical sensors, and wearable sensors.[97] In their review, Pang *et al.* categorized sensors into "anthropomorphic" senses: sight, hearing, smell, taste, touch, space, and balance. They also reviewed actuators designed for stimulating muscles, which employ MXene-based films or membranes in combination with other functional materials.[98] The MXene-derived image sensors as artificial retinas, gas sensors, chemical biosensors, acoustic devices, and tactile sensors for electronic skin were all discussed.[98] Wu *et al.* then systematically summarized the application of $Ti_{n+1}C_nT_x$ in nine categories of sensors such as strain, gas, and light sensors.[95] MXenes are also finding use in emerging intelligent and bionic devices, including smart flexible devices, bionic E-skin, neural

network coding and learning, bionic soft robots, as well as in an intelligent artificial eardrum.[95] For the applications of MXene in biosensors, the optical and electrical properties at the sub-nano and nano scale are most important;[1] at the meso and micro scale, mechanical properties become important as well.[1] All these properties can be employed for electrochemical, optical and/or wearable sensors. In general, MXenes can be exfoliated before their subsequent applications; for example, they can be doped into other polymers to form composite nanoparticles, thin films or fibers.[99] In this review we will focus on the recent publications on electrochemical sensors (for small molecules, DNA/RNA or proteins, up to microorganisms), optical sensors, and wearable and *in situ* engineering sensors.

5.1. The applications of MXenes in electrochemical (bio)sensors

The large surface area, tunable electrical properties, excellent mechanical strength, good dispersibility, and biocompatibility of MXenes make them attractive for bio-electrochemical sensing platforms.[100] Kalambate *et al.* reviewed the progress of electrochemical (bio) sensors for the detection of biomarkers, pharmaceutical drugs, and environmental contaminants, including how the synthetic strategies and surface functionalization affect various properties of MXenes.[101] Many other excellent recent reviews of MXene-based sensors are also available,[102–111] and this work provides updates through 2023.

Table 1 lists electrochemical MXene-based sensors for small molecules published in 2023. MXene (especially Ti_3C_2) and other conductive nanomaterials (typically gold nanoparticles) have been used for the sensing of hydrogen peroxide,[112–114] Aflatoxin B1,[115–117] chlorpyrifos,[118–120] and glucose[121–124] with sensing ranges in nM to mM and limits of detection in pM to μM ranges. A specific receptor for the detection of some small molecules is not always required; often their characteristic redox potentials are sufficient. Notably, sensing platforms for chlorpyrifos[120] or methotrexate[125] employed field effect transistors. Cui *et al.* developed non-enzymatic glucose sensors by modifying Au@CuO/V_2CT_x MXene nanocomposites (NCs) on the surface of a disposable laser-induced graphene (LIG) electrode.[122] These sensors have excellent electrocatalytic activity for glucose oxidation in an alkaline medium,[122] and they achieved a detection range of 0.005 to 5.0 mM and a limit of detection (LOD) of 1.8 μM.[122] The sensor had good selectivity and stability (84.12% activity retained after 6 weeks).[122] Zhang *et al.* constructed a sensitive sweat biosensor for ascorbic acid (AA) quantification built on a heterostructure with 3D linked network microstructures made from 2D MoS_2 nanosheets and Ti_3C_2 MXene.[126] The inherent conductivity, extremely porous structure, and active catalytic properties of 2D/2D heterostructures showed enhanced electrocatalytic activity toward the oxidation of ascorbic acid to achieve a detection limit of 4.2 μM.[126] Wu *et al.* designed strongly coupled molybdenum sulfide (MoS_2)/MXene hybrids for constructing an efficient electrocatalytic biomimetic sensor.[127] Their results show that interfacial stresses, atomic defects, and an adjustable inter-sheet spacing between MoS_2/MXene nanosheets significantly promote biomolecular adsorption and rapid electron transfer, resulting in excellent electrochemical activity and reaction kinetics.[127] The $MoS_2/Ti_3C_2T_x$ modified electrode shows a sensitivity of 1.2 μA μM^{-1} for dopamine detection with a low detection limit of 0.05 μM.[127] Vilian *et al.* integrated gold nanoparticles (AuNPs) into polypyrrole (PPy) on titanium carbide MXene ($Ti_3C_2T_x$) using a sonochemical route involving the *in situ*, oxidant-free polymerization of pyrrole monomers in the presence of $HAuCl_4$.[128] Au-PPy-MXene-GCE exhibited better electrocatalytic reduction performance at a higher cathodic signal intensity and a lower reduction overpotential of −0.38 V (*vs.* Ag/AgCl) for nitrofurantoin (NFT) than Au-MXene, Au-PPy, and PPy-MXene GCEs.[128] The fabricated sensor had a wide linear range from 6 to 172 nM, and an ultra-low detection limit (LOD) of 0.26 nM for the electroreduction of NFT.[128]

Recent publications on MXene-based electrochemical sensors for DNA/RNA or proteins are listed in Table 2. In general, gold nanoparticles are incorporated, especially for the conjugation of DNA probes.[144–148] The sensing range for miRNA,[144–146] DNA/RNA,[147,149] or genes[148] is lower than ∼nM. For the sensing of proteins (*e.g.*, cTnI,[150,151] H5N1 viral proteins,[152] IL-6[153,154] or Sortase A[142]), detection limits reach as low as ∼fg mL^{-1}. Receptors are required on the surface of electrodes to ensure specificity and selectivity for these targets. Vessella *et al.* developed a novel V_2CT_x MXene-based immunosensor for the rapid and accurate detection of interleukin-6 (IL-6).[153] The modified V_2CT_x tag was captured by the electrode surface with cysteamine to detect the analyte, IL-6, after being attached with a capture antibody.[153] Our previous work used three novel peptides for epitope imprinting; Ti_2C doping dramatically increased the sensing range (for C-reactive protein) from 0.1 to 100 fg mL^{-1} to 10 000 fg mL^{-1} with only a very small concentration of MXene (*e.g.*, Ti_2C at 0.1 wt% in the preparation solution).[155]

5.2. The applications of MXenes in optical (bio)sensors

Optical sensing applications with MXenes, began with colorimetric,[156,157] fluorescent,[156,158–164] chemiluminescence (ECL),[165–171] and surface plasmon resonance (SPR) detection[172–177] and are summarized in Table 3; in recent years, photoelectrochemical (PEC) detection[178–186] and surface-enhanced Raman scattering (SERS) detection have been added.[159,187–189] Their metallic conductivity, rich surface chemistry, hydrophilicity, good biocompatibility, and high anchoring capacity for biomaterials make them an attractive candidate for detecting a variety of analytes.[190] In a review by Babar *et al.*, it was proposed that the hexagonal stacking network of MXenes acts as a distinctive host matrix for nanoparticles; the embedded nanoparticles can bind more biomolecules (*e.g.*, antibodies), thereby improving biosensor performance.[190] With the surface conjugation of receptors, MXene quantum dot (MQD) sensors are a promising platform for identifying target analytes by sensing fluorescence, electrochemical signals, or photoluminescence.[191]

Table 1 Electrochemical MXene-based sensors for small molecules

Electrode	Surface modification	Signal enhancer	Method	Receptor	Analyte	Sensing range	Detection limit	Ref.
GCE	HIL/Ti_3C_2		CA	Hemoglobin	H_2O_2	2.0 nM–27.2 μM	2.0 nM	112
	MXene-Co_3O_4		LSV		H_2O_2	0–75 μM	0.5 μM	113
ITO	PB-MXene		CA		H_2O_2	1 μM–500 μM	0.57 μM	114
GCE	rGO/$Ti_3C_2T_x$		DPV	MIPs	Acetaminophen	10 nM–1.0 mM	1.58 nM	129
GCE	Au@Mxene		CA	RLM	Aflatoxin B1	0.01 μM–50 μM	2.8 nM	115
SGPGE	MXene/MWCNTs/$NiCo_2O_4$/PDA		DPV	Apt	Aflatoxin B1	2.5–200 ng mL^{-1}	1.89 ng mL^{-1}	116
SPE	$Ti_3C_2T_x$/Au		DPV	Ab	Aflatoxin B1	10 pg mL^{-1}–1.0 μg mL^{-1}	1.62 pg mL^{-1}	117
SPE	$Ti_3C_2T_x$/Au		DPV	Apt	Ampicillin	10 pM–500 nM	2.28 pM	117
CP	$Ti_3C_2T_x$/MoS_2		CV		Ascorbic acid	10–5000 μM	4.2 μM	126
GCE	V_2O_5@$Ti_3C_2T_x$		DPV		Bisphenol A	414 nM–31.2 μM	87 nM	130
GCE	MXenes/PEI-MWCNTs		CA	CSDBLac	Catechol	1–1000 μM	0.15 μM	131
GCE	MXene/Fe@Ti-MOF-NH_2/pTHi		SWV	MIPs	Catechol	1.0–4000 mM	0.54 μM	132
AuE	AuNPs/MXene		SWV	Peptide	Cathepsin B	3.9–250 nM	0.62 nM	133
GCE	MXene/AuPt		DPV	AChE	Chlorpyrifos	1.0 pg mL^{-1}–1.0 μg mL^{-1}	1.55 pg mL^{-1}	118
GCE	SnO_2/Nb_2CT_x		DPV	AChE	Chlorpyrifos	51 fM–510 nM	51 fM	119
	PEDOT:PSS-Ti_2CT_x-BSA-GO		P-ISFET		Chlorpyrifos		0.95 μM	120
GCE	MXene/SA/SiO_2@C22 MEPCM		CA	Chox	Cholesterol	0.6–48.6 μM	0.081 μM	134
SPE	MXene-MWCNTs		DPV		Cortisol	0.1 fg mL^{-1}–1 μg mL^{-1}	0.03 fg mL^{-1}	135
ITO	1T-MoS_2/$Ti_3C_2T_x$		DPV		Dopamine	0.1–40 μM	0.05 μM	127
3DE	MXene QDs		CV		Dopamine	0.01–20 μM	3 nM	136
GCE	MXene/MOF		DPV		Flutamide	0.05–70 μM	0.015 μM	137
SPE	$Ti_3C_2T_x$/Au		DPV	Ab	Fumonisin B1	10 pg mL^{-1}–1 μg mL^{-1}	1.62 pg mL^{-1}	117
GCE	Cu_2O/Mxene/rGO		CA		Glucose	0.1–40 mM	1.1 μM	121
LIG	Au@CuO/V_2CT_x		CA	Gox	Glucose	5.0 μM–5.0 mM	1.8 μM	122
GCE	$Ti_3C_2T_x$/graphene/AuNPs		CV	Gox	Glucose	2 μM–6 mM	2 μM	123
SPE	MXene@CeO_2		DPV		Glucose	1.0–2.5 μM	4 nM	124
GCE	MXene/TiO_2/Nafion		LS-AdsSV		Capsaicin	0.05–25 μM	25 nM	138
GCE	MXenes/PEI-MWCNTs		CA	CSDBLac	Hydroquinone	1.0 μM–1.24 mM	0.09 μM	131
GCE	MXene/VS_2	SA-$CeCu_2O_4$ NPs	SWV	DNA	Kanamycin	5 pM–5 μM	0.6 pM	139
	MWCNTs-doped MXene		MMSFETs	Apt	Methotrexate	1.0 nM–100 μM	0.35 nM	125
GCE	AuNPs/Ti3C2T_x		FET		Nitrite	0.01 nM–5 mM	0.01 nM	140
GCE	AuNP-PPy-MXene		LSV		Nitrofurantoin	6–172 nM	0.26 nM	128
GCE	Ag-$Ti_3C_2T_x$/CNTs		DPV		Paracetamol	0.01–35.0 μM	3.4 M	141
PI	MXene/AuNPs		DPV	Peptide	Pyocyanin	1–100 μM		142
SPCE	MXene–chitosan		CV	SOx	Sarcosine	5–50 μM	7.0 nM	143

Abbreviations: GCE: glassy carbon electrode; ITO: indium tin oxide; SGPGE: surface-graphenized pencil graphite electrode; SPE: screen-printed electrodes; CP: carbon paper; AuE: gold electrode; 3DE: 3D electrode; LIG: laser-induced graphene; PI: polyimide; HIL: hydrophobic ionic liquid; PB: Prussian blue; rGO: reduced graphene oxide; MWCNTs: multi-walled carbon nanotubes; PDA: polydopamine; PEI: polyetherimide; MOF: metal–organic framework; pTHi: poly(thionine); AuNPs: gold nanoparticles; PEDOT: poly(3,4-ethylenedioxythiophene); PSS: poly(styrenesulfonate); BSA: bovine serum albumin; GO: graphene oxide; SA: sodium alginate; MEPCM: microencapsulated phase change materials; QDs: quantum dots; PPy: polypyrrole; CA: chronoamperometry; LSV: linear sweep voltammetry; DPV: differential pulse voltammetry; SWV: square wave voltammetry; P-ISFET: P-channel ion-sensitive field-effect transistor; LS-AdsSV: linear sweep-adsorptive stripping voltammetry; MMSFETs: multi-spiral-channel field-effect transistor; FET: field-effect transistor; MIPs: molecularly imprinted polymer; RLM: rat liver microsomes; Apt: aptamer; Ab: antibody; CSDBLac: cell surface-displayed BLac; AChE: acetylcholinesterase; Chox: choline oxidase; Gox: glucose oxidase; and Sox: sarcosine oxidase.

Kong *et al.* prepared Ti_3C_2 MXene to stimulate peroxidase activity and quench fluorescence,[156] which, when labeled with Aflatoxin B1 (AFB1) aptamers and 6-carboxyfluorescein (FAM), was used to construct a novel multimode biosensor for the detection of AFB1 in peanuts. This fluorescence/colorimetric/smart phone detection of AFB1 achieved detection limits in the range of about 0.09 to 0.96 ng mL^{-1}.[156] Wu *et al.* developed a ratiometric surface-enhanced Raman scattering (SERS) aptasensor for AFB1 detection, in which 1,2-bis(4-pyridyl) ethylene (BPE) was used to trigger the assembly of Au nanoparticle dimers (AuNP dimers) and form intense SERS ''hotspots''; MXenes nanosheets could be loaded with aptamer-modified AuNP dimers due to hydrogen bonding and chelation between the phosphate groups of aptamers and the Ti ion of MXenes.[193] With the binding of AFB1 to the aptamer, AuNP dimers were separated from MXenes nanosheets, leading to a decrease in SERS intensity, providing a sensing range from 0.001 to 100 ng mL^{-1} and a limit of detection of 0.6 pg mL^{-1}.[193] Wei *et al.* reported an ECL amplification system consisting of SnS_2 quantum dots decorated with Ti_3C_2 MXene nanocomposites as the energy donor, which exhibited highly efficient NIR ECL emission due to the surface-defect effect generated by the oxygen-containing functional groups in MXene.[166] Nonmetallic plasma hydrated defective tungsten oxide nanosheets ($dWO_3 \cdot H_2O$) were utilized as energy acceptors because of their strong surface plasmon resonance effect in the vis-NIR absorption range.[166] The tetracycline (TCN) aptamer and its complementary chain served as a bridge to connect the energy donor and acceptor, allowing the successful construction of a NIR ECL-RET aptasensor.[166] This ECL

Table 2 Electrochemical MXene-based sensors for DNA/RNA or proteins

Electrode	Surface modification	Signal enhancer	Method	Receptor	Analyte	Sensing range	Detection limit	Ref.
GCE	Mxene-rGO-Au	Mxene-AuPd	DPV	ssDNA	miRNA-21	1 fM–1 nM	0.42 fM	144
GCE	Au HFGNs/PnBA-MXene		DPV	ssDNA	miRNA-122	0.01 aM–10 nM	0.0035 aM	145
GCE	MXene/AuNPs	MCH	SWV	ssDNA	miRNA-155	5 fM–5 nM	1.2 fM	146
GCE	MXene/Pt/C	RNA-MB	DPV	ssDNA	DNA/RNA	1 aM–100 nM	0.4 aM	149
SPE	Ti_3C_2/AuNPs		SWV	CRISPR-Cas12a	HPV18 DNA	10 pM–500 nM	1.95 pM	147
GCE	Au NPs@Ti_3C_2	MCH	SWV	DNA duplex	KRAS gene	10 fM–10 nM	0.38 fM	148
AuE	Ti_3C_2/MWCNTs		DPV	Apt	cTnI	10 pg mL^{-1}–1.0 μg mL^{-1}	6.21 pg mL^{-1}	150
ITO	AuNPs/Ti_3C_2		DPV	Apt	cTnI	0.24 fg mL^{-1}–24 ng mL^{-1}	0.14 fg mL^{-1}	151
AuE	BSA/MXene		SWV	Peptide	H5N1 viral proteins	0.48–500 nM	0.10 nM	152
AuE	V_2CT_x/PB/Au NPs		DPV	Ab	IL-6	0.005–0.5 ng mL^{-1}	0.5 pg mL^{-1}	153
Cr/Au	Ti_3C_2		SiMFETs	Apt	IL-6	10 fg mL^{-1}–100 ng mL^{-1}	2.34 fg mL^{-1}	154
PI	MXene/AuNPs		DPV	Peptides	Sortase A	1 pg mL^{-1}–100 ng mL^{-1}		142
ITO		MXene	CV	MIPs	CRP	0.1–10000 fg mL^{-1}	0.2 ag mL^{-1}	155

Abbreviations: GCE: glassy carbon electrodes; AuE: gold electrode; ITO: indium tin oxide; PI: polyimide; rGO: reduced graphene oxide; HFGNs: hierarchical flower-like gold nanostructures; PnBA: poly(*n*-butyl acrylate); MWCNTs: multi-walled carbon nanotubes; BSA: bovine serum albumin; PB: Prussian blue; DPV: differential pulse voltammetry; SWV: square wave voltammetry; SiMFETs: spiral interdigitated MXene–assisted field effect transistor; CV: cycle voltammetry; ssDNA: single-stranded DNA; CRISPR-Cas12a: clustered regularly interspaced short palindromic repeats-CRISPR associated protein 12a; Apt: aptamer; Ab: antibody; MIPs: molecularly imprinted polymers; HPV18: human papilloma virus 18; KRAS: Kirsten rat sarcoma viral oncogene homolog; cTnI: cardiac troponin I; H5N1: influenza A virus subtype H5N1; IL-6: interleukin 6; and CRP: C-reactive protein.

sensing platform had a detection limit of 6.2 fM with a linear range from 10 fM to 10 μM.[166]

Yang *et al.* combined high-load hybridization probes targeting nucleocapsid phosphoprotein and OFR1a polyprotein genes with Au NPs@MXene (Ta_2C) modified gold-coated tilted fiber Bragg grating (TFBG) sensors to enable direct nucleic acid detection.[176] Multiple activation sites of SARS-CoV-2 were modified on the surface of a homogeneous array of AuNPs@Ta_2C(MXene)/Au.[176] The system demonstrates a limit of detection of 0.2 pg mL^{-1}, with a rapid response time of 1.5 min for clinical samples without amplification.[176] Hung *et al. in situ* hybridized Zr-based ultrathin metal–organic layers (Zr-TCBPE-MOL, H4TCBPE = 1,1,2,2-tetra(4-carboxylbiphenyl) ethylene) with highly conductive $Ti_3C_2T_x$ MXene nanosheets to obtain a unique 2D-2D hybrid nanocomposite (Zr-TCBPE-MOL/MXene).[168] The resulting Zr-TCBPE-MOL/MXene nanocomposite permitted fast electron/ion transport across the whole framework of Zr-TCBPE-MOL/MXene, which efficiently boosted the electrochemical activation of TCBPE luminophores, resulting in a remarkable ECL emission.[168] This Zr-TCBPE-MOL/MXene-based ECL microRNA-141 sensor exhibited a response range from 100 aM to 1.0 nM and a detection limit of 16.2 aM.[168] In a signal amplification strategy, PtCo@Prussian blue nanozyme was selected as a signal nanoprobe with high catalytic activity and large specific surface area, while two dimensional MXene/AuNPs as a surface modification material was applied to improve the active sites of the electrode.[146] This miR-155 biosensor shows a low limit of detection of 1.2 fM and a sensing range of 5 fM to 5 nM.[146] Li *et al.* developed an ECL biosensor based on bimetallic MXene derivative QDs (Mo_2TiC_2 QDs) and SnS_2 nanosheets/lipid bilayers to detect the gastric cancer marker miRNA-27a-3p.[167] The inter-band excitation of Mo_2TiC_2 QDs can inject additional carriers, which were less suppressed by boundary effects making a significant contribution to the luminescence process.[167] SnS_2 nanosheets coated with a phospholipid bilayer were designed as the sensing interface. SnS_2 nanosheets not only enhanced the luminous intensity of Mo_2TiC_2 QDs by virtue of their large surface area and low dielectric constant, but also improved the stability of the lipid bilayer.[167] This biosensor displayed a good linear correlation between the ECL intensity and the concentration of miRNA-27a-3p over a wide range from 1 fM to 10 nM with a detection limit as low as 1 fM.[167]

Zhou *et al.* designed a cyclic voltammetry (CV)/electrochemiluminescence (ECL) dual-mode electrochemical biosensor based on multi-functionalized 2D MXene@Fe_3O_4-APTs and BPNS@CuNPs-APTs as the capture/signal unit, respectively, for the detection of lung cancer (A549) circulating tumor cells (CTCs).[171] The linear range and the detection limit of both CV and ECL were 10–10^6 and 3 cells per mL, respectively.[171] Shi *et al.* synthesized an ultrasensitive TiO_2/MXene/CdS QD (TiO_2/MXene/CdS) heterostructure as a photoelectrochemical immunosensor, which favors energy level matching and fast electron transfer from CdS to TiO_2 with the help of an ultrathin MXene nanosheet.[183] Dramatic photocurrent quenching can be observed upon incubation of the TiO_2/MXene/CdS electrode in Cu^{2+} solution in a 96-well microplate, which was caused by the formation of CuS and subsequent cupric sulfates Cu_xS (x = 1, 2), reducing the absorption of light and boosting electron–hole recombination upon irradiation.[183] The biosensor demonstrated linearly increasing photocurrent quenching with CEA concentration ranging from 1 fg mL^{-1} to 10 ng mL^{-1}, along with a low detection limit of 0.24 fg mL^{-1}.[183] Yang *et al.* used a highly sensitive and portable photothermal cytosensor for the direct capture and quantification of breast cancer circulating tumor cells (BC-CTCs).[192] Ti_3C_2@Au@Pt nanocomposites were selectively bound to the BC-CTC surface through multi-aptamer recognition, which enhanced the specificity and facilitated signal amplification.[192] Zhou *et al.* used a sonochemical method to grow Ag_2S nanoparticles (NPs) on ZnO nanowire

Table 3 MXene-based optical biosensors

Surface modification	Signal enhancer	Method	Receptor	Analyte	Sensing range	Detection limit	Ref.
Ti_3C_2 nano-enzymes		Colorimetric	ssDNA	AFB1	0.1–400.0 ng mL^{-1}	0.09 ng mL^{-1}	156
$Pt/Ti_3C_2T_x$		Colorimetric		HIV-DNA		0.1 nM	157
N-Ti_3C_2 NQDs	Ce^{4+}/*o*-phenylenediamine	FL	*o*-phenylenediamine	Ascorbic acid	2–240 μM	0.82 μM	158
MSN–NH_2	R6G	FL	Apt	AFB1	0.001–100 ng mL^{-1}	0.214 pg mL^{-1}	159
Ti_3C_2 nano-enzymes		FL	ssDNA	AFB1	1.0–700.0 ng mL^{-1}	0.61 ng mL^{-1}	156
Ti_3C_2	Apt-1/Apt-2/Cas12a	FL	ssDNA-FAM	AFB1	1.0 pg mL^{-1}–80 ng mL^{-1}	0.92 pg mL^{-1}	160
N-Ti_3C_2 NQDs	Ce^{4+}/*o*-phenylenediamine	FL		Acid phosphatase	0.15–3.75 U L^{-1}	0.02 U L^{-1}	158
Carboxymethyl cellulose sodium-functionalized Nb_2C MXene	Tb-Norfloxacin coordination polymer nanoparticles	FL	Ab	HE4	10 fg mL^{-1} to 10 ng mL^{-1}	3.3 fg mL^{-1}	161
FL-V_2CT_x	GODs	FL	Apt	PSA	0.1 to 20 ng mL^{-1}	0.03 ng mL^{-1}	162
Ti_3C_2-QD		FL		FluA		2.4 pg mL^{-1}	163
Ti_3C_2-QD		FL		SARS-CoV-2		6.2 pg mL^{-1}	163
Au NPs	MXene	FL	Apt1/Apt2	Exosomes	100 to 10^7 particles per μL	42 particles per μL	164
MXene-Nafion		ECL		H_2O_2	10 nM–1.0 mM	3.1 nM	165
SnS_2 QDs-Ti_3C_2	NH_2-dWO_3·H_2O-cDNA	NIR ECL-RET	Apt	Tetracycline	10 fM–10 μM	6.2 fM	166
Mo_2TiC_2 QDs		ECL	ssDNA	miRNA-27a-3p	1 fM–10 nM	1 fM	167
Zr-TCBPE/$Ti_3C_2T_x$/AuNPs		ECL	DNA walker	microRNA-141	100 aM–1 nM	16.2 aM	168
Au atoms-Mxene	H_2O_2	ECL	Ab	Myeloperoxidase	0.01–10 ng mL^{-1}	3 pg mL^{-1}	169
Zn-TCPP-TiO2–Ti_3C_2	TPrA@AuNPs	ECL	Apt1/Apt2	Exosomes	100–1.0 × 10^5 particles per μL	11 particles per μL	170
MXene@Fe_3O_4		ECL	Apt	A549	10–1.0 × 10^8 cells per mL	3 cells per mL	171
AuNPs/Nb_2CT_x		LSPR	Tyrosinase	Tyramine	0–300 μM	0.35μM	172
2D MXene		SPR		BSA		10 fM	173
Gold/MXene/MOF		SPR		Haemoglobin	100–500 μg mL^{-1}		174
CG@MXene		SPR	CRISPR/Cas12a	S. Typhimurium	160–1.6 × 10^7 CFU mL^{-1}	160 CFU mL^{-1}	175
AuNPs@Ta_2C		SPR	ssDNA	SARS-CoV-2		0.2 pg mL^{-1}	176
SnS_2@Ti_3C_2	$Ru(NH_3)_6^{3+}$	PEC	BDNA	5-Carboxycytosine	1 pM to 0.2 μM	260 fM	178
$TiO_2/Ti_3C_2T_x$		PEC		Folate	100–2 × 10^7 cells per mL	1.01 cells per mL	179
MOF/MXene		PEC	PCN-224(Zn)	Dimethoate	0.1 nM to 1000 nM	26.1 pM	180
$Ti_3C_2T_x$ MXene/Ag_2S		PEC	DNA tetrad	miRNA-141	100 aM to 100 pM	34 aM	181
TiO_2/Ti_3C_2/Au NPs	QDs/MCH	PEC	Probe DNA	DNA	10 nM–10 fM	6 fM	182
SnS_2@Ti_3C_2		PEC		DNA carboxylation	1 pM–0.2 μM	260 fM	178
TiO2/MXene/CdS QDs	CuO NF	PEC	Ab1/Ab2	CEA	1 fg mL^{-1}–10 ng mL^{-1},	0.24 fg mL^{-1}	183
Ag_2S on ZnO-MXene		PEC	Ab	Silk	5.0 pg mL^{-1}–50 ng mL^{-1}	1.51 pg mL	184
Bi_2S_3/Ti_3C_2	CTS/CuO	PEC	Apt	Microcystin-RR	0.1 fM–10 pM	0.047 fM	185
H-TiO_2/Ti_2CO_X		PEC		Microcystic toxins-LR	10^{-9}–10^3 μg L^{-1}	1 fg L^{-1}	186
Nb_2C-Au NPs		SERS		Adenine		50 nM	187
MXene/AuNPs	R6G	SERS		AFB1	0.5 pg mL^{-1}–100 ng mL^{-1}	0.133 pg mL^{-1}	159
Ti_3C_2	Au NPs	SERS	Apt	Isocarbophos	1.0 pM–2.5 pM	45 fM	188

Table 3 (*continued*)

Surface modification	Signal enhancer	Method	Receptor	Analyte	Sensing range	Detection limit	Ref.
$Ti_3C_2T_x$	Au@MPBA@SiO_2	SERS	Peptide	ExoPD-L1	100–5 × 10^6 particles per mL	20.74 particles per mL	189
$Ti_3C_2T_x$/AuNPs	TMB/H_2O_2	UV/Vis		Penicillin G	35.1–584 nM	7.51 nM	177
Ti_3C_2@Au@Pt	TMB	UV/Vis	Apt	BC-CTCs	50–1.0 × 10^5 cells per mL	50 cells per mL	192
Ti_3C_2 nano-enzymes		Smart phone	ssDNA	AFB1	1.00–800.00 ng mL^{-1}	0.96 ng mL^{-1}	156

Abbreviations: NQDs: N-doped quantum dot; MSN: mesoporous silica nanoparticle; QD: quantum dot; Au NPs: gold nanoparticles; MOFs: metal–organic framework; R6G: rhodamine 6G; GODs: glucose oxidase; TPrA: tripropylamine; MCH: 6-mercaptohexanol; NF: nanofibers; CTS: chitosan; MPBA: mercaptophenylboric acid; TMB: 3,3′,5,5′-tetramethylbenzidine; FL: fluorescent; ECL: electrogenerated chemiluminescence; NIR: near-infrared; RET: resonance energy transfer; LSPR: localized surface plasmon resonance; SPR: surface plasmon resonance; PEC: photoelectrochemical; SERS: surface-enhanced Raman scattering; OECT: organic electrochemical transistors; Apt: aptamer; ssDNA: single-stranded DNA; FAM: 6-carboxyfluorescein; Ab: antibody; CRISPR/Cas12a: clustered regularly interspaced short palindromic repeats (CRISPR)/CRISPR-associated (Cas) protein 12a; BDNA: branched DNA; PCN-224: porphyrin Zr metal–organic framework; AFB1: Aflatoxin B1; HE4: human epididymis protein 4; PSA: prostate-specific antigen; FluA: influenza A; A549: human lung carcinoma; BSA: bovine serum albumin; CEA: carcinoembryonic antigen; ExoPD-L1: exosomal PD-L1; BC-CTCs: breast cancer circulating tumor cells; and ALP: alkaline phosphatase.

array-MXene nanocomposites (ZnO-MX) to form aphotosensitive substrates, Fig. 7.[184] Then, a taxonomically specific antifibroin monoclonal antibody was prepared and employed in a visible/near-infrared (vis/NIR) photoelectrochemical (PEC) immunosensor.[184] The ZnO-MX/Ag_2S-based sensor exhibited 6.8 times-larger PEC responses than a ZnO-MX-based sensor under visible light illumination, and the PEC signal of the ZnO-MX/Ag_2S nanocomposites was 30 times as high as that of ZnO-MX under 808 nm NIR light.[184] This PEC immunosensor exhibited a linear range of 0.005–50 ng mL^{-1} and a low detection limit of 1.51 pg mL^{-1}.[184]

5.3. The Applications of MXenes in microorganism sensors

The unique surface chemistries with abundant functional termini, excellent conductivity, tunable electric and optical attributes and a high specific surface area have made MXenes an ideal material for application in virus-diagnosing biosensors.[194] Two excellent reviews cover (1) MXene-based virus-detecting biosensors, their limitations, potential solutions, and advanced intelligent prospects with the integration of internet-of-things, artificial intelligence, 5G communications, and cloud computing technologies;[194] and (2) the advances in the development of sensors for the detection of SARS-CoV-2, exploiting the exceptional properties of 2D materials.[195] Electrochemical sensors for microorganisms using MXene-based nanomaterials are summarized in Table 4. Exosomes,[196–199] bacteria,[200–205] viruses,[149,206–209] and even cancer cells[114,171] can be measured through appropriate surface modification of electrodes. The lowest sensing range is about 10 particles per μL.

Virus-detecting biosensors may detect virus-specific biomolecules, or sense whole microorganisms.[194] Chen *et al.* used electrodes made of MXene–AuNP composites for improved sensitivity and the CRISPR/Cas13a system for high specificity in detecting the single-base L452R mutation (in the SARS-Cov-2 virus) in RNAs and clinical samples.[208] Kim *et al.* developed a field-ready cyanobacterial pretreatment device and an electrochemical clustered regularly interspaced short palindromic repeats (EC-CRISPR) biosensor.[200] The biosensor was composed of CRISPR/Cpf1 protein conjugated with MXene on an Au microgap electrode (AuMGE) integrated into a printed circuit board (PCB).[200] Using the extracted M. aeruginosa gene with a pre-treatment filter, the CRISPR biosensor showed a limit of detection of 89.0 pg mL^{-1} in fresh water.[200]

Chen *et al.* developed a novel nanozyme-mediated electrochemical aptasensor for tuberculosis diagnosis; hemin decorated with multi-layered MXene enhanced the metal–support interaction with nano-gold *via* charge transfer, resulting in excellent peroxidase-like activity.[203] *Mycobacterium tuberculosis* (MTB)-specific ESAT-6 antigen aptamers with MXene@hemin-Au as probes for signal amplification and gold nanoparticles supported on nitrogen-doped carbon nanotubes (N-CNTs-Au) were used as a sensing platform.[203] The sensor exhibited a wide linear detection range for ESAT-6 antigens from 100 fg mL^{-1} to 50 ng mL^{-1} with a limit of detection of 2.36 fg mL^{-1}.[203]

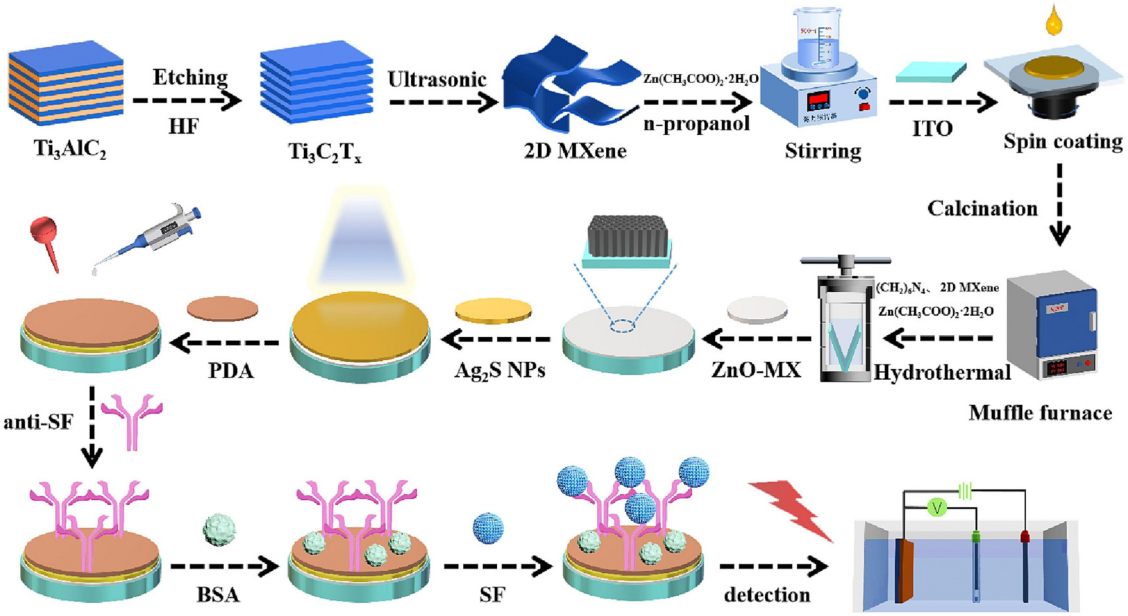

Fig. 7 The synthesis process of ZnO-MX/Ag_2S composites and the fabrication process for the PEC immunosensor. Reprinted with permission from Elsevier, copyright 2023.[184]

Table 4 MXene-based electrochemical biosensors for microorganisms

Electrode	Surface modification	Signal enhancer	Method	Receptor	Analyte	Sensing range	Detection limit	Ref.
GCE	MXenes-Au NPs	MCH	DPV	Apt	Exosome surface proteins	100–5 × 10^6 particles per μL	10^4 particles per μL	196
GCE	Au NPs/$Ti_3C_2T_x$		DPV	Apt	Exosomes	100–5 × 10^5 exosomes per μL	20 exosomes per μL	197
GCE	Fe_3O_4–NH_2	Ti_3C_2	DPV	Apt1/Apt2	Exosomes	100–10^7 particles per μL	43 particles per μL	198
PU/2-FPBA	Mxene-GO	Au NPs	DPV	Apt	Exosomes	50–10^5 particles per μL	42 particles per μL	199
AuMGE	Mxene		CV	EC-CRISPR	Cyanobacteria	0.1 ng mL^{-1}–1 μg mL^{-1}	89.0 pg mL^{-1}	200
ITO	Mxenes	Phage-Apo@CuO_2	SWV	AMP	*E. coli*	10–10^8 CFU mL^{-1}	6 CFU mL^{-1}	201
GCE	MXene@Au	MB-PEI-Van	DPV		MRSA	38–3.8 × 10^7 CFU mL^{-1}	38 CFU mL^{-1}	202
GCE	Au@BP@Ti_3C_2	Au@$ZnFe_2O_4$@COF	DPV	Peptide/Apt	NoV	10–10^8 copies per μL	3 copies per μL	206
GCE	HFGNs/MXene/PPY	MB	DPV	ssDNA	Rotavirus	1.0 aM–100 nM	0.8 aM	209
GCE	CG@MXene		DPV	E-CRISPR/ssDNA	*S. Typhimurium*	160–1.6 × 10^7 CFU mL^{-1}	160 CFU mL^{-1}	204
GCE	MXene/Pt/C	MB-RNA	DPV	ssDNA	SARS-CoV-2	1.0 aM–100 nM	0.4 aM	149
SPE	FL-$Ti_3C_2T_x$-NS		DPV	Ab	SARS-CoV-2		0.91 nM	207
AuE	MXene-AuNP		DPV	CRISPR/Cas13a	SARS-CoV-2 variants	1.0 nM–10 fM	1.72 pM	208
GCE	AuNPs/$Ti_3C_2T_x$		DPV	CIPs	Yeast cells	10^2–1.0 × 10^9 cells per mL	20 cells per mL	205
GCE	N-CNTs-Au	MXene@hemin-Au	CA	Apt	Tuberculosis	100 fg mL^{-1}–50 ng mL^{-1}	2.36 fg mL^{-1}	203
MGCE	MXene@Fe_3O_4		FSCV	Apt	A549	10–10^8 cells per mL	3 cells per mL	171
ITO	PB-MXene		DPV	anti-CEA	CTCs	13–1.3 × 10^6 cells per mL	9 cells per mL	114

Abbreviations: GCE: glassy carbon electrodes; PU: polyurethane; 2-FPBA: 2-formylphenylboronic acid; AuMGE: Au microgap electrode; ITO: indium tin oxide; SPE: screen-printed electrode; AuE: gold electrode; Au NPs: gold nanoparticles; GO: graphene oxide; BP: black phosphorous; HFGNs: hierarchical flower-like gold nanostructures; PPY: polypyrrole; CG: colloidal gold; FL: few layer; NS: nanosheet; N-CNTs: N-doped carbon nanotubes; PB: prussian blue; MCH: 6-mercaptohexanol; phage-Apo: phage-apoferritin; MB: methylene blue; PEI: polyethyleneimine; Van: vancomycin; COF: covalent organic framework; DPV: differential pulse voltammetry; CV: cycle voltammetry; SWV: square wave voltammetry; CA: chronoamperometry; FSCV: fast-scan cyclic voltammetry; Apt: aptamer; EC-CRISPR: electrochemical biosensor based on CRISPR/Cas12a; AMP: antimicrobial peptide; ssDNA: single-stranded DNA; CRISPR/Cas13a: clustered regularly interspaced short palindromic repeats/CRISPR associated protein 13a; CIPs: cell-imprinted polymers; anti-CEA: carcinoembryonic antigen antibody; MRSA: methicillin-resistant *Staphylococcus aureus*; NoV: norovirus; A549: human lung carcinoma; and CTCs: circulating tumor cells.

Zhou *et al.* have presented an approach for the specific identification and analysis of exosomal programmed cell death protein–ligand 1 (ExoPD-L1) through the non-selective trapping effect of $Ti_3C_2T_x$ MXene on exosomes *via* the formation of Ti–O–P complexation, and the selective capture of peptide-functionalized Au@MPBA (4-mercaptophenylboronic acid)@SiO_2 surface

enhanced Raman scattering (SERS) tags on ExoPD-L1.[189] The biosensor delivered both a hypersensitive and reliable performance in exosome detection with a low limit of detection (21 particles per mL) in the linear range of 10^2 to 5×10^6 particles per mL.[189] Xiao *et al.* developed a phage-apoferritin@CuO_2 (phage-Apo@CP) probe on an antimicrobial peptide (AMP)/MXenes-modified detection platform.[201] With the specific recognition of AMP and phage-Apo@CP, the biosensor for the target *Escherichia coli* O157:H7 (*E. coli* O157:H7) presented multi-mode (bioluminescent, colorimetric, and electrochemical) signals to simultaneously measure live and dead bacteria.[201] The bioluminescent signal generated by the adenosine triphosphate (ATP) from the bacteria was used to quantify live bacteria. The colorimetric and voltammetric signals triggered by $^{\bullet}OH$ and Cu^{2+} from the probe with the assistance of acid could rapidly screen and quantitatively determine the total concentration of *E. coli* O157:H7.[201] The biosensor was successfully used for on-site measurement of live and dead *E. coli* O157:H7 in food samples with a limit of detection of 30 colony-forming unit CFU mL^{-1} for live ones and 6 CFU mL^{-1} for total bacteria within 50 min.[201] Li *et al.* introduced a magnetic separation-based electrochemical biosensor for the detection of methicillin-resistant *Staphylococcus aureus* (MRSA).[202] Vancomycin (Van) was used to modify the surface of polyethyleneimine (PEI) mediated MBs (MBs-PEI-Van) for the separation and enrichment of MRSA.[202] MXene@Au with a controllable size of AuNPs was synthesized by a self-reduction method and employed to modify the glassy carbon electrode (GCE).[202] Immunoglobulin G (IgG) was loaded onto the modified electrode to immobilize MRSA, and ferroceneboronic acid (Fc-BA) was used as a probe for quantitative determination.[202] The differential pulse voltammetry (DPV) current was plotted against the concentration of MRSA from 3.8×10^1 to 3.8×10^7 CFU mL^{-1} with a limit of detection (LOD) of 3.8×10^1 CFU mL^{-1}.[202] In addition, MRSA was successfully detected in spiked cerebrospinal fluid (CSF) samples with satisfactory recoveries (94–107%) and validation results (RSD $< 11\%$).[202]

5.4. Applications of MXenes in wearable and *in situ* sensors

MXenes have emerged as a unique class of layered-structured metallic materials with attractive features, such as good conductivity comparable to metals, enhanced ionic conductivity, hydrophilicity from their hydroxyl or oxygen-terminated surfaces, and mechanical flexibility.[210] Monolayer titanium carbide (Ti_3C_2) MXenes are widely used for sensing applications; these MXenes have a 330 ± 30 GPa modulus, 2.31 ± 0.57 μΩ m electrical resistivity, and 2.6 ± 0.7 cm^2 V^{-1} s^{-1} field-electron mobility. Grabowski reviewed the sensing capabilities of MXene nanomaterials for structural health monitoring (SHM)

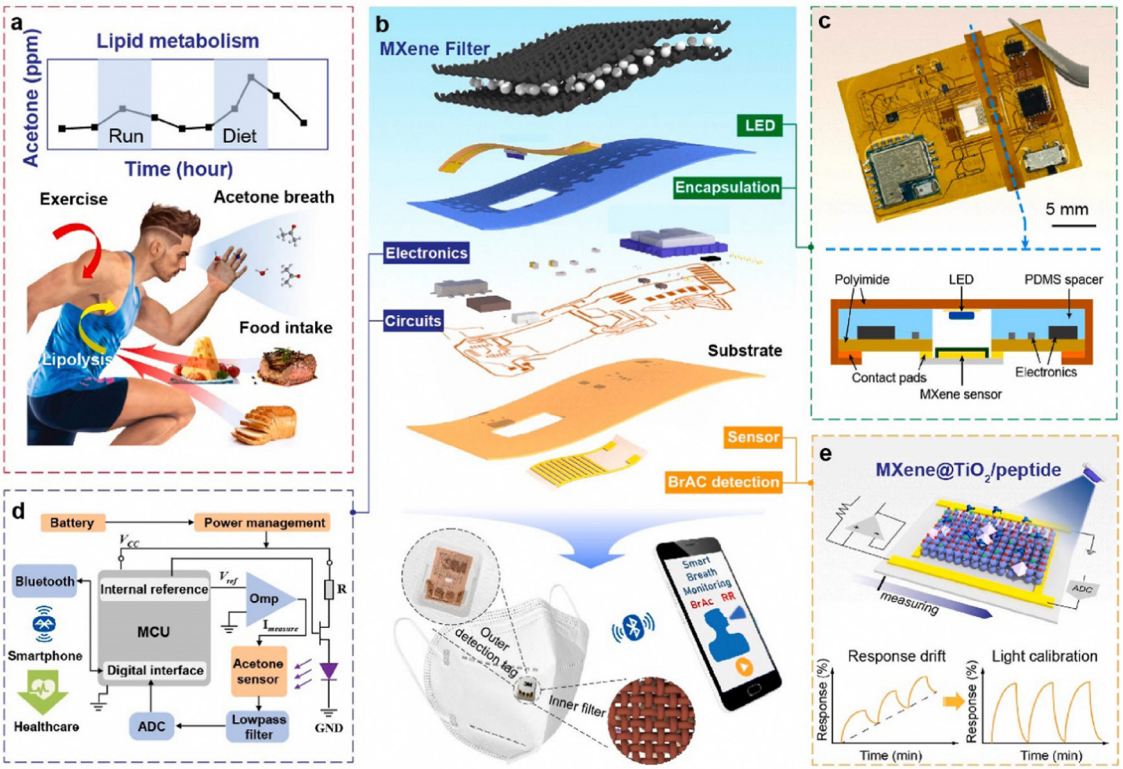

Fig. 8 Hierarchical design of the MXene-based facemask platform for wearable breath acetone detection and metabolic monitoring of lipids.[212] (a) The influence of diet and exercise upon breath acetone levels.[212] (b) The inner side of the facemask is functionalized by the filter while the flexible detection tag can be amounted at the outlet of the breath valve.[212] (c) The integrated detection tag for breath acetone sensing: photograph of the detection tag (25 × 35 mm) and cross-sectional illustration of the assembled tag.[212] (d) Block diagram of the sensing system. VCC, powering voltage. Vref, reference voltage. Omp, operational amplifier. Imeasure, measuring current. MCU, microcontroller. ADC, analog-digital converter. (e) Schematic illustration of acetone sensing using a light-calibrated MXene sensor.[212] Reprinted with permission from Elsevier, copyright 2023.[212]

of engineering structures (including measurements of strain, pressure, impact, or temperature).[1] With appropriate design, MXene (or MXene composite) sensors show enhanced mechanical flexibility and stretchability, enabling their wide application in the fields of wearable sensors, energy storage, and electromagnetic shielding.[210] Xin *et al.* summarized applications in wearable sensors including pressure/strain sensing, biochemical sensing, temperature, and gas sensing; sources of uncertainties in both physical sensors and computational models were discussed along with the effect of MXene material properties on measurement concepts like repeatability, reliability, and error estimation, *etc.*, of the sensors.[1]

Zhao and co-workers developed a hybrid MXene-laden cellulose fabric and showed its potential for humidity-responsive applications for drug delivery. In their study, a commercial cellulose substrate was immersed in a high-concentration MXene aqueous solution (5 mg mL^{-1}). After a vacuum drying process at 60 °C, the MXene nanosheets can be coated on the cellulose fibers to form a flexible MXene-laden fabric, and the MXene nanosheets present on cellulose fibers conferredelectrical conductivity properties to the commercial cellulose fabrics through their design. In addition to enhancing conductivity, MXene nanosheets contain abundant hydrophilic bioactive sites and possess a large specific surface area, which provide a moisture-capturing capability to MXene-laden cellulose fabrics.[211] The MXene-laden cellulose fabrics exhibit an electro-thermal transition behavior, making the fabrics humidity-responsive and offering a potential application where the fabrics can exhibit H_2O-induce swelling/contraction behaviors driven by the electro-thermal transition properties. Such swelling/contraction can be used to control drug release. Li *et al.* reported a $Ti_3C_2T_x$ MXene-based wireless facemask for on-body breath acetone (BrAC) detection and real-time tracking of lipid metabolism, where $Ti_3C_2T_x$ MXene serves as a versatile nanoplatform for not only acetone detection but also breath filtration, Fig. 8.[212] The incorporation of *in situ* grown TiO_2 and short peptides with $Ti_3C_2T_x$ MXene further improves the acetone sensitivity and selectivity.[212] Through a hierarchically designed filtration–detection–calibration–transmission system, the BrAC detection can be quantified down to 0.31 ppm in breath.[212] Zhang *et al.* developed a wearable self-powered toroidal triboelectric sensor (STTS) with a pyramidal structure for self-powered interactions.[213] The pyramidal structure of the nanocomposite and flexible conductive fabric electrodes assembled with 3D-printed gloves based on the flexible TPU material maintained the wearability of the sensing system.[213] The high peak-to-peak voltage (19.91 V), high sensitivity (0.088 Vk Pa^{-1}), and wide pressure detection range (0–120 kPa) enable the generation of high-quality output signals for the accurate detection of various finger movements.[213]

6. Conclusions and future prospects

In this review, recent applications of MXenes in biomedicine and sensing have been surveyed, showing the great potential of these materials. Compared to the high-pressure- or high-temperature-based manufacturing process of other 2D materials, such as MoS_2 or black phosphorus, MXenes can be synthesized in a relatively gentle environment at room temperature. MXene efficacy in a wide variety of applications consistently hinges upon the elemental composition and structural disposition of the atoms in them.[214] This underscores that the synthetic pathways constitute pivotal factors in crafting MXenes endowed with the desired properties. In addition, because of the well-defined general structural features and composition of MXenes, several high-throughput theoretical methods for screening MXene properties and compositions have been reported recently. Mixed composition surface functionalization has been investigated for various MXenes, including Ti_2CT_x, $Ti_3C_2T_x$, Nb_2CT_x, and $Nb_4C_3T_x$ (T = O, F, and OH). The O-terminated MXenes are identified as the most stable, while OH-terminated MXenes show a tendency to decompose. A computational screening of $M_{n+1}X_nT_x$ MXenes in an H_2SO_4 electrolyte revealed 24 MXene candidates suitable for electrode utilization. Nitride-based MXenes generally exhibit superior capacitive performance compared to carbides.[215] In addition, the surface functional groups also affect the electronic and thermal transport in MXenes. By introduction of functional groups, the synthesized MXene can be dissolved in water-based aqueous solutions, making it suitable for cell culture and various biomedical applications. However, numerous challenges still persist at present. For example, the negative ion-rich MXene surface may result in a lower uptake as well as a non-homogenous internalization on the cell surface, thus decreasing the therapeutic effects on cancer cells.[66] The same study also showed that cells cultured with high MXene concentration can maintain high cell viability when treated with photothermal therapy. It is possible that aggregation at high Mxene concentration adversely affects the uptake into cells and the photothermal therapy effect. Nanoparticle shape is another factor that may affect biomedical applications. For example, previous studies indicated that spherical nanoparticles are more readily taken up by cells than rod-shaped nanomaterials.[102] Finally, the need for large-scale clinical production with cost-effectiveness remains a hurdle, along with ensuring the stability of nanoparticles. Structural defects lead to instability of MXene nanomaterials in an oxygen-rich environment and may lead to degradation of MXene structures when exposed to biological fluids.[216,217] Furthermore, these changes alter the performance of MXene-based materials and result in safety issues in biomedical applications. MXene modification or multiple material hybridization may offer a strategy to create more stable nanoparticles. Improving the stability holds great potential for the applications of MXene-based stimuli-responsive materials in the design of kinetic soft robotics and smart bioactuators in different environments.

MXene provides superior biocompatibility and hydrophilicity compared to other 2D materials. MXene's highly negative zeta potential ensures stable colloidal dispersions in diverse solvents, preventing aggregation. Its expanded specific surface area facilitates effective drug loading, and its intrinsic

antimicrobial properties support biological implantation. However, the concentration-dependent safety impact on normal cells necessitates careful consideration. Strategic surface functionalization/modification may enhance MXene's dispersibility, fortify its loading capacity, decrease cytotoxicity, and increase biocompatibility, closely aligning it with the requirements of biomedical applications. In addition, ensuring long-term stability and understanding their potential environmental impacts are vital concerns. So, before widespread clinical adoption, rigorous testing for their biosafety and biocompatibility is necessary. Importantly, it is required to comprehensively study the interaction of MXenes with biological systems and their long-term effects. To address these stability challenges, researchers must further optimize the structure of MXene, develop more stable derivatives, or design protective coatings or encapsulation strategies to safeguard MXene from detrimental influences within the biological environment. In addition, further refinement of MXene synthesis conditions and surface modifications to reduce toxicity and extend its stability within the circulatory system should contribute to its biomedical advancements. Understanding the cellular uptake behavior of MXene-based materials and the influence of surface functionalization on biocompatibility is crucial for advancing biomedical research. Further investigations are imperative to thoroughly explore the pharmacokinetics, long-term toxicity, and biodistribution of MXene, encompassing diverse animal models for comprehensive insights. In recent research on the applications of MXene in electrochemical biosensors, there is a notable trend towards targeting larger entities like proteins or microorganisms, and there is an increased use of optical sensors employing ECL, SPR, PEC or SERS methods.

In conclusion, while MXenes offer exciting prospects in biomedicine, addressing these challenges will be crucial to unlock their full potential for improving human health and healthcare practices. As ongoing research overcomes the current challenges and extends our understanding of the properties and potential applications of MXene and its derivatives, MXene is poised to play a significant role in advancing biomedical technologies and improving healthcare outcomes.

Conflicts of interest

There are no conflicts to declare.

Acknowledgements

The authors would like to appreciate the National Science and Technology Council, Taiwan, no. MOST 109-2314-B-390-001-MY3, MOST 110-2221-E-390-003-MY3, MOST 110-2221-E-214-012 and MOST 111-2221-E-214-001-MY3.

References

1 K. Grabowski, S. Srivatsa, A. Vashisth, L. Mishnaevsky Jr. and T. Uhl, *Measurement*, 2022, **189**, 110575.
2 G. Deysher, C. E. Shuck, K. Hantanasirisakul, N. C. Frey, A. C. Foucher, K. Maleski, A. Sarycheva, V. B. Shenoy, E. A. Stach and B. Anasori, *ACS Nano*, 2019, **14**, 204–217.
3 J. Chen, W. Fu, F.-L. Jiang, Y. Liu and P. Jiang, *J. Mater. Chem. B*, 2023, **11**, 702–715.
4 R. Garg and F. Vitale, *MRS Bull.*, 2023, **48**, 283–290.
5 M. Qin, C. Merzougui, Y.-M. Su, Y.-F. Li, W.-Y. Chen and D. Huang, *New Carbon Mater.*, 2023, **38**, 496–506.
6 M. Naguib, M. W. Barsoum and Y. Gogotsi, *Adv. Mater.*, 2021, **33**, 2103393.
7 Z. Sun, Q. Fan, M. Zhang, S. Liu, H. Tao and J. Texter, *Adv. Sci.*, 2019, **6**, 1901084.
8 Z. Huang, X. Cui, S. Li, J. Wei, P. Li, Y. Wang and C.-S. Lee, *Nanophotonics*, 2020, **9**, 2233–2249.
9 H. Lin, Y. Wang, S. Gao, Y. Chen and J. Shi, *Adv. Mater.*, 2018, **30**, 1703284.
10 X. Han, X. Jing, D. Yang, H. Lin, Z. Wang, H. Ran, P. Li and Y. Chen, *Theranostics*, 2018, **8**, 4491.
11 X. Han, J. Huang, H. Lin, Z. Wang, P. Li and Y. Chen, *Adv. Healthcare Mater.*, 2018, **7**, 1701394.
12 Y. Zhu, Z. Wang, R. Zhao, Y. Zhou, L. Feng, S. Gai and P. Yang, *ACS Nano*, 2022, **16**, 3105–3118.
13 H. Lin, S. Gao, C. Dai, Y. Chen and J. Shi, *J. Am. Chem. Soc.*, 2017, **139**, 16235–16247.
14 X. Han, X. Jing, D. Yang, H. Lin, Z. Wang, H. Ran, P. Li and Y. Chen, *Theranostics*, 2018, **8**, 4491–4508.
15 Y. Xu, Y. Wang, J. An, A. C. Sedgwick, M. Li, J. Xie, W. Hu, J. Kang, S. Sen, A. Steinbrueck, B. Zhang, L. Qiao, S. Wageh, J. F. Arambula, L. Liu, H. Zhang, J. L. Sessler and J. S. Kim, *Bioactive Mater.*, 2022, **14**, 76–85.
16 X. Yang, C. Zhang, D. Deng, Y. Gu, H. Wang and Q. Zhong, *Small*, 2022, **18**, e2104368.
17 G. H. Yang, F. L. Liu, J. Y. Zhao, L. J. Fu, Y. Q. Gu, L. L. Qu, C. Z. Zhu, J. J. Zhu and Y. H. Lin, *Coordin. Chem. Rev.*, 2023, **479**, 215002.
18 T. T. Hu, Z. Gu, G. R. Williams, M. Strimaite, J. J. Zha, Z. Zhou, X. C. Zhang, C. L. Tan and R. Z. Liang, *Chem. Soc. Rev.*, 2022, **51**, 6126–6176.
19 X. Yuan, J. Shi, Y. Kang, J. Dong, Z. Pei and X. Ji, *Adv. Mater.*, 2023, DOI: **10.1002/adma.202308726**.
20 B. Li, D. Chu, H. Cui, Z. Li, Z. Zhou, C. Tan and J. Li, *SmartMat*, 2023, e1243, DOI: **10.1002/smm2.1243**.
21 Y. X. Bian, X. J. Cai, Z. H. Lv, Y. M. Xu, H. Wang, C. L. Tan, R. Z. Liang and X. S. Weng, *Adv. Sci.*, 2023, **10**, 2301806.
22 W. Shen, T. Hu, X. Liu, J. Zha, F. Meng, Z. Wu, Z. Cui, Y. Yang, H. Li, Q. Zhang, L. Gu, R. Liang and C. Tan, *Nat. Commun.*, 2022, **13**, 3384.
23 T. Hu, W. Shen, F. Meng, S. Yang, S. Yu, H. Li, Q. Zhang, L. Gu, C. Tan and R. Liang, *Adv. Mater.*, 2023, **35**, e2209692.
24 W.-J. Zhang, S. Li, Y.-Z. Yan, S. S. Park, A. Mohan, I. Chung, S.-K. Ahn, J. R. Kim and C.-S. Ha, *Int. J. Mol. Sci.*, 2022, **23**, 14925.
25 J. D. Hayes, A. T. Dinkova-Kostova and K. D. Tew, *Cancer Cell*, 2020, **38**, 167–197.
26 Y. Wang, H. Qi, Y. Liu, C. Duan, X. Liu, T. Xia, D. Chen, H.-L. Piao and H.-X. Liu, *Theranostics*, 2021, **11**, 4839.

27 A. Bansal and M. C. Simon, *J. Cell Biol.*, 2018, **217**, 2291–2298.
28 B. Lin, H. Chen, D. Liang, W. Lin, X. Qi, H. Liu and X. Deng, *ACS Appl. Mater. Interfaces*, 2019, **11**, 11157–11166.
29 Y. S. Choi, K. M. Huh, M. S. Shim, I. S. Park, Y.-Y. Cho, J. Y. Lee, H. S. Lee and H. C. Kang, *Adv. Funct. Mater.*, 2021, **31**, 2007275.
30 W. A. Catterall, G. Wisedchaisri and N. Zheng, *Nat. Chem. Biol.*, 2017, **13**, 455–463.
31 A. H. Rajabi, M. Jaffe and T. L. Arinzeh, *Acta Biomater.*, 2015, **24**, 12–23.
32 H. Huang, C. Dong, W. Feng, Y. Wang, B. Huang and Y. Chen, *Adv. Drug Delivery Rev.*, 2022, **184**, 114178.
33 N. H. Solangi, S. A. Mazari, N. M. Mubarak, R. R. Karri, N. Rajamohan and D.-V. N. Vo, *Environ. Res.*, 2023, **222**, 115337.
34 L. Mao, S. Hu, Y. Gao, L. Wang, W. Zhao, L. Fu, H. Cheng, L. Xia, S. Xie, W. Ye, Z. Shi and G. Yang, *Adv. Healthcare Mater.*, 2020, **9**, e2000872.
35 O. Ajiteru, K. Y. Choi, T. H. Lim, H. Hong, Y. J. Lee, J. S. Lee, H. Lee, Y. J. Suh, M. T. Sultan and O. J. Lee, *Biofabrication*, 2021, **13**, 034102.
36 S. M. George and B. Kandasubramanian, *Ceram. Int.*, 2020, **46**, 8522–8535.
37 M. Liao, Q. Cui, Y. Hu, J. Xing, D. Wu, S. Zheng, Y. Zhao, Y. Yu, J. Sun and R. Chai, *Neural Regener. Res.*, 2024, **19**, 258–263.
38 R. Guo, M. Xiao, W. Zhao, S. Zhou, Y. Hu, M. Liao, S. Wang, X. Yang, R. Chai and M. Tang, *Acta Biomater.*, 2022, **139**, 105–117.
39 H. Rastin, B. Zhang, A. Mazinani, K. Hassan, J. Bi, T. T. Tung and D. Losic, *Nanoscale*, 2020, **12**, 16069–16080.
40 W. Wu, H. Ge, L. Zhang, X. Lei, Y. Yang, Y. Fu and H. Feng, *Chem. Res. Toxicol.*, 2020, **33**, 2953–2962.
41 R. Guo, M. Xiao, W. Zhao, S. Zhou, Y. Hu, M. Liao, S. Wang, X. Yang, R. Chai and M. Tang, *Acta Biomater.*, 2022, **139**, 105–117.
42 N. Driscoll, A. G. Richardson, K. Maleski, B. Anasori, O. Adewole, P. Lelyukh, L. Escobedo, D. K. Cullen, T. H. Lucas, Y. Gogotsi and F. Vitale, *ACS Nano*, 2018, **12**, 10419–10429.
43 Z. Zhang, S. Gao, Y.-N. Hu, X. Chen, C. Cheng, X.-L. Fu, S.-S. Zhang, X.-L. Wang, Y.-W. Che, C. Zhang and R.-J. Chai, *Adv. Sci.*, 2022, **9**, 2203557.
44 M. Liao, Y. Hu, Y. Zhang, K. Wang, Q. Fang, Y. Qi, Y. Shen, H. Cheng, X. Fu, M. Tang, S. Sun, X. Gao and R. Chai, *ACS Nano*, 2022, **16**, 16744–16756.
45 Z. Zhang, S. Gao, Y. N. Hu, X. Chen, C. Cheng, X. L. Fu, S. S. Zhang, X. L. Wang, Y. W. Che and C. Zhang, *Adv. Sci.*, 2022, **9**, 2203557.
46 J. Cai, H. Zhang, Y. Hu, Z. Huang, Y. Wang, Y. Xia, X. Chen, J. Guo, H. Cheng, L. Xia, W. Lu, C. Zhang, J. Xie, H. Wang and R. Chai, *J. Nanobiotechnol.*, 2022, **20**, 460.
47 E. J. Berns, S. Sur, L. Pan, J. E. Goldberger, S. Suresh, S. Zhang, J. A. Kessler and S. I. Stupp, *Biomaterials*, 2014, **35**, 185–195.
48 Y. D. Zhu, X. Y. Ma, L. P. Li, Q. J. Yang, F. Jin, Z. N. Chen, C. P. Wu, H. B. Shi, Z. Q. Feng and S. K. Yin, *Adv. Healthcare Mater.*, 2023, 2300731.
49 L.-P. Nan, Z. Lin, F. Wang, X.-H. Jin, J.-Q. Fang, B. Xu, S.-H. Liu, F. Zhang, Z. Wu, Z.-F. Zhou, F. Chen, W.-T. Cao, J.-G. Wang and J.-J. Liu, *Front. Bioeng. Biotechnol.*, 2022, 10.
50 Y. Li, Y. Hu, H. Wei, W. Cao, Y. Qi, S. Zhou, P. Zhang, H. Li, G.-L. Li and R. Chai, *J. Nanobiotechnol.*, 2022, **20**, 398.
51 M. Xiao, X. Li, S. Pifferi, B. Pastore, Y. Liu, M. Lazzarino, V. Torre, X. Yang, A. Menini and M. Tang, *Nanoscale*, 2022, **14**, 10992–11002.
52 F. Qi, R. Liao, P. Wu, H. Li, J. Zan, S. Peng and C. Shuai, *Mater. Chem. Front.*, 2023, **7**, 1671–1683.
53 Y. Wang, R. Garg, J. E. Hartung, A. Goad, D. A. Patel, F. Vitale, M. S. Gold, Y. Gogotsi and T. Cohen-Karni, *ACS Nano*, 2021, **15**, 14662–14671.
54 G. A. Roth, G. A. Mensah, C. O. Johnson, G. Addolorato, E. Ammirati, L. M. Baddour, N. C. Barengo, A. Z. Beaton, E. J. Benjamin, C. P. Benziger, A. Bonny, M. Brauer, M. Brodmann, T. J. Cahill, J. Carapetis, A. L. Catapano, S. S. Chugh, L. T. Cooper, J. Coresh, M. Criqui, N. DeCleene, K. A. Eagle, S. Emmons-Bell, V. L. Feigin, J. Fernandez-Sola, G. Fowkes, E. Gakidou, S. M. Grundy, F. J. He, G. Howard, F. Hu, L. Inker, G. Karthikeyan, N. Kassebaum, W. Koroshetz, C. Lavie, D. Lloyd-Jones, H. S. Lu, A. Mirijello, A. M. Temesgen, A. Mokdad, A. E. Moran, P. Muntner, J. Narula, B. Neal, M. Ntsekhe, G. Moraes de Oliveira, C. Otto, M. Owolabi, M. Pratt, S. Rajagopalan, M. Reitsma, A. L. P. Ribeiro, N. Rigotti, A. Rodgers, C. Sable, S. Shakil, K. Sliwa-Hahnle, B. Stark, J. Sundstrom, P. Timpel, I. M. Tleyjeh, M. Valgimigli, T. Vos, P. K. Whelton, M. Yacoub, L. Zuhlke, C. Murray, V. Fuster and G.-N.-J. G. B. O. C. D. W. Group, *J. Am. Coll. Cardiol.*, 2020, **76**, 2982–3021.
55 F. Sanchis-Gomar, C. Perez-Quilis, R. Leischik and A. Lucia, *Ann. Transl. Med.*, 2016, **4**, 256.
56 L. C. Liew, B. X. Ho and B. S. Soh, *Stem Cell Res. Ther.*, 2020, **11**, 138.
57 M. F. Tenreiro, A. F. Louro, P. M. Alves and M. Serra, *NPJ Regen. Med.*, 2021, **6**, 30.
58 C. Gokce, C. Gurcan, L. G. Delogu and A. Yilmazer, *Front. Cardiovasc. Med.*, 2022, **9**, 802551.
59 J. Lee, V. Manoharan, L. Cheung, S. Lee, B. H. Cha, P. Newman, R. Farzad, S. Mehrotra, K. Zhang, F. Khan, M. Ghaderi, Y. D. Lin, S. Aftab, P. Mostafalu, M. Miscuglio, J. Li, B. B. Mandal, M. A. Hussain, K. T. Wan, X. S. Tang, A. Khademhosseini and S. R. Shin, *ACS Nano*, 2019, **13**, 12525–12539.
60 B. Guo and P. X. Ma, *Biomacromolecules*, 2018, **19**, 1764–1782.
61 M. Malki, S. Fleischer, A. Shapira and T. Dvir, *Nano Lett.*, 2018, **18**, 4069–4073.
62 P. Hitscherich, A. Aphale, R. Gordan, R. Whitaker, P. Singh, L. H. Xie, P. Patra and E. J. Lee, *J. Biomed. Mater. Res. A*, 2018, **106**, 2923–2933.
63 S. R. Shin, S. M. Jung, M. Zalabany, K. Kim, P. Zorlutuna, S. B. Kim, M. Nikkhah, M. Khabiry, M. Azize, J. Kong,

K. T. Wan, T. Palacios, M. R. Dokmeci, H. Bae, X. S. Tang and A. Khademhosseini, *ACS Nano*, 2013, **7**, 2369–2380.
64 C. Liao, Y. Li and S. C. Tjong, *Int. J. Mol. Sci.*, 2018, **19**, 3564.
65 K. P. Steckiewicz, E. Barcinska, A. Malankowska, A. Zauszkiewicz–Pawlak, G. Nowaczyk, A. Zaleska-Medynska and I. Inkielewicz-Stepniak, *J. Mater. Sci.: Mater. Med.*, 2019, **30**, 1–15.
66 M. Aghaleh, A. Rafiee, M. H. Morowvat and Y. Ghasemi, *Mater. Today Commun.*, 2021, **29**, 102979.
67 B. B. Murphy, P. J. Mulcahey, N. Driscoll, A. G. Richardson, G. T. Robbins, N. V. Apollo, K. Maleski, T. H. Lucas, Y. Gogotsi and T. Dillingham, *Adv. Mater. Technol.*, 2020, **5**, 2000325.
68 A. Rafieerad, W. Yan, G. L. Sequiera, N. Sareen, E. Abu-El-Rub, M. Moudgil and S. Dhingra, *Adv. Healthcare Mater.*, 2019, **8**, e1900569.
69 G. Ye, Z. Wen, F. Wen, X. Song, L. Wang, C. Li, Y. He, S. Prakash and X. Qiu, *Theranostics*, 2020, **10**, 2047.
70 G. Basara, M. Saeidi-Javash, X. Ren, G. Bahcecioglu, B. C. Wyatt, B. Anasori, Y. Zhang and P. Zorlutuna, *Acta Biomater.*, 2022, **139**, 179–189.
71 T. Y. Hou, Z. G. Li, F. Luo, Z. Xie, X. H. Wu, J. C. Xing, S. W. Dong and J. Z. Xu, *Biomaterials*, 2014, **35**, 5689–5699.
72 Y. Wang, W. G. Cui, X. Zhao, S. Z. Wen, Y. L. Sun, J. M. Han and H. Y. Zhang, *Nanoscale*, 2019, **11**, 60–71.
73 L. P. Tong, Q. Liao, Y. T. Zhao, H. Huang, A. Gao, W. Zhang, X. Y. Gao, W. Wei, M. Guan, P. K. Chu and H. Y. Wang, *Biomaterials*, 2019, **193**, 1–11.
74 I. S. Aleem, I. Aleem, N. Evaniew, J. W. Busse, M. Yaszemski, A. Agarwal, T. Einhorn and M. Bhandari, *Sci. Rep.*, 2016, **6**, 31724.
75 K. Xiong, T. Wu, Q. Fan, L. Chen and M. Yan, *ACS Appl. Mater. Interfaces*, 2017, **9**, 44356–44368.
76 C.-H. Yao, B.-Y. Yang and Y.-C. E. Li, *Front. Bioeng. Biotechnol.*, 2022, **10**, 832808.
77 J. Zhang, Y. Fu and A. Mo, *Int. J. Nanomed.*, 2019, **14**, 10091–10103.
78 Z. C. Hu, J. Q. Lu, T. W. Zhang, H. F. Liang, H. Yuan, D. H. Su, W. Ding, R. X. Lian, Y. X. Ge, B. Liang, J. Dong, X. G. Zhou and L. B. Jiang, *Bioact. Mater.*, 2023, **22**, 1–17.
79 M. Samie, A. F. Khan, J. G. Hardy and M. A. Yameen, *Macromol. Biosci.*, 2022, **22**, e2200219.
80 X. Zhao, H. Qiu, Y. Shao, P. Wang, S. Yu, H. Li, Y. Zhou, Z. Zhou, L. Ma and C. Tan, *Acta Phys.-Chim. Sin.*, 2023, **39**, 2211043.
81 B. Li, D. Chu, H. Cui, Z. Li, Z. Zhou, C. Tan and J. Li, *SmartMat*, 2023, e1243.
82 S. Pandit, S. Karunakaran, S. K. Boda, B. Basu and M. De, *ACS Appl. Mater. Interfaces*, 2016, **8**, 31567–31573.
83 I. Y. Kim, S. Park, H. Kim, S. Park, R. S. Ruoff and S.-J. Hwang, *Adv. Funct. Mater.*, 2013, **24**, 2288–2294.
84 B. Xue, X. Geng, H. Cui, H. Chen, Z. Wu, H. Chen, H. Li, Z. Zhou, M. Zhao and C. Tan, *Chin. Chem. Lett.*, 2023, 108140.
85 Y. Zhao, C. J. Wang, W. Gao, B. Li, Q. Wang, L. Zheng, M. Wei, D. G. Evans, X. Duana and D. O'Hare, *J. Mater. Chem. B*, 2013, **1**, 5988–5994.
86 Y. Zheng, X. Hong, J. Wang, L. Feng, T. Fan, R. Guo and H. Zhang, *Adv. Healthcare Mater.*, 2021, **10**, e2001743.
87 X. Zhu, Y. Zhu, K. Jia, B. S. Abraha, Y. Li, W. Peng, F. Zhang, X. Fan and L. Zhang, *Nanoscale*, 2020, **12**, 19129–19141.
88 H. Zheng, S. Wang, F. Cheng, X. He, Z. Liu, W. Wang, L. Zhoua and Q. Zhang, *Chem. Eng. J.*, 2021, **424**, 130148.
89 K. Rajavel, S. Shen, T. Ke and D. Lin, *Appl. Surf. Sci.*, 2021, **538**, 148083.
90 J. Li, Z. Li, X. Liu, C. Li, Y. Zheng, K. W. K. Yeung, Z. Cui, Y. Liang, S. Zhu, W. Hu, Y. Qi, T. Zhang, X. Wang and S. Wu, *Nat. Commun.*, 2021, **12**, 1224.
91 S. Iravani and R. S. Varma, *RSC Adv.*, 2023, **13**, 9665–9677.
92 K. Rasool, K. A. Mahmoud, D. J. Johnson, M. Helal, G. R. Berdiyorov and Y. Gogotsi, *Sci. Rep.*, 2017, **7**, 1598.
93 A. A. Shamsabadi, M. S. Gh, B. Anasori and M. Soroush, *ACS Sustainable Chem. Eng.*, 2018, **6**, 16586–16596.
94 R. P. Pandey, P. A. Rasheed, T. Gomez, K. Rasool, J. Ponraj, K. Prenger, M. Naguib and K. A. Mahmoud, *ACS Appl. Nano Mater.*, 2020, **3**, 11372–11382.
95 L. Wu, X. Yuan, Y. Tang, S. Wageh, O. A. Al-Hartomy, A. G. Al-Sehemi, J. Yang, Y. Xiang, H. Zhang and Y. Qin, *PhotoniX*, 2023, **4**, 15.
96 Z. Jing, J. Liu, N. Li, H. Wang, K. Wu, Y. Cheng and B. Xiao, *J. Phys. D: Appl. Phys.*, 2020, **54**, 015301.
97 V. A. Tran, N. T. Tran, V. D. Doan, T.-Q. Nguyen, H. H. P. Thi and G. N. Vo, *Micromachines*, 2023, **14**, 247.
98 J. Pang, S. Peng, C. Hou, X. Wang, T. Wang, Y. Cao, W. Zhou, D. Sun, K. Wang and M. H. Rümmeli, *Nano Res.*, 2023, **16**, 5767–5795.
99 W. Eom, H. Shin, R. B. Ambade, S. H. Lee, K. H. Lee, D. J. Kang and T. H. Han, *Nat. Commun.*, 2020, **11**, 2825.
100 S. Ganesan, K. Ramajayam, T. Kokulnathan and A. Palaniappan, *Molecules*, 2023, **28**, 4617.
101 P. K. Kalambate, N. S. Gadhari, X. Li, Z. Rao, S. T. Navale, Y. Shen, V. R. Patil and Y. Huang, *TrAC, Trends Anal. Chem.*, 2019, **120**, 115643.
102 T. Yu and C. B. Breslin, *J. Electrochem. Soc.*, 2019, **167**, 037514.
103 X. Wu, P. Ma, Y. Sun, F. Du, D. Song and G. Xu, *Electroanalysis*, 2021, **33**, 1827–1851.
104 C. Laghlimi, A. Moutcine, A. Chtaini, J. Isaad, A. Soufi, Y. Ziat, H. Amhamdi and H. Belkhanchi, *ADMET and DMPK*, 2023, **11**, 151–173.
105 W. Wang and S. Gunasekaran, *Biosensors*, 2022, **12**, 982.
106 H. Fernández, M. A. Zon, S. A. Maccio, R. D. Alaníz, A. Di Tocco, R. A. Carrillo Palomino, J. A. Cabas Rodríguez, A. M. Granero, F. J. Arévalo and S. N. Robledo, *Biosensors*, 2023, **13**, 694.
107 N. Chandrasekar, A. P. Steffi, B. Ramachandran, M. T. Hwang, V. Faramarzi and M. Govarthanan, *Environ. Res.*, 2023, 115900.

108 X. Yuan, M. Zhang and Y. Wu, *Sens. Mater.*, 2020, **32**, 4047–4065.
109 R. S. Chouhan, M. Shah, D. Prakashan, P. R. Ramya, P. Kolhe and S. Gandhi, *Diagnostics*, 2023, **13**, 697.
110 R. Manisekaran, A.-D. R. Chettiar, G. Kandasamy, R. Garcia-Contreras and L. S. Acosta-Torres, *Biomater. Adv.*, 2023, 213354.
111 L. Lorencova, K. K. Sadasivuni, P. Kasak and J. Tkac, *Novel Nanomaterials*, IntechOpen, 2020.
112 R. Gao, Y. Song, Y. Gao, X. Yang and S.-J. Bao, *Sens. Actuators Rep.*, 2023, **5**, 100146.
113 S. Singh, A. Numan, M. Khalid, I. Bello, E. Panza and S. Cinti, *Small*, 2023, 2208209.
114 X. Su, Q. You, L. Zhuang, Z. Chang, M. Ge, L. Yang and W.-F. Dong, *J. Pharm. Biomed. Anal.*, 2023, 115479.
115 X. Sun, J. Sun, Y. Ye, J. Ji, L. Sheng, D. Yang and X. Sun, *Bioelectrochemistry*, 2023, **151**, 108378.
116 J. Shen, J. Liu, S. Yang, X. Yao, H. Fa, C. Hou and M. Yang, *Food Anal. Methods*, 2023, 1–14.
117 W. Wang, Y. Yin and S. Gunasekaran, Available at SSRN 4401739.
118 R. Ding, W. Jiang, Y. Ma, Q. Yang, X. Han and X. Hou, *Microchem. J.*, 2023, **187**, 108425.
119 W. Guo, L. Liang, Y. Zhao, C. Zhao, X. Lu, Y. Cao and F. Gao, *Colloids Surf., B*, 2023, **224**, 113238.
120 M. M. Hasnan, G. Lim, N. Nayan, C. Soon, A. A. Halim, M. Ahmad, S. Said, M. M. Ali and I. Noor, *Polym. Bull.*, 2023, **80**, 1243–1264.
121 A. Nirmala Grace, T. S. Gopal, M. Muthuramamoorthy, A. A. E. Alobaidi, R. Abdullah Alsaigh, M. Hamad Aldosary, S. Pandiaraj and A. Alodhayb, Available at SSRN: **https://ssrn.com/abstract=4408347**.
122 F. Cui, H. Sun, X. Yang, H. Zhou, Y. Wu, J. Li, H. Li, J. Liu, C. Zeng and B. Qu, *Chem. Eng. J.*, 2023, **457**, 141303.
123 L. Feng, W. Qin, Y. Wang, C. Gu, X. Li, J. Chen, J. Chen, H. Qiao, M. Yang and Z. Tian, *Microchem. J.*, 2023, **184**, 108142.
124 S. Jiang, H. Zhang, Z. Li, L. Chen, L. Yin and X. Liu, *Mater. Today Chem.*, 2023, **32**, 101638.
125 C. Lu, P. Xu, D. Wang and D. Fu, *Arabian J. Chem.*, 2023, **16**, 104943.
126 Y. Zhang, Z. Wang, X. Liu, Y. Liu, Y. Cheng, D. Cui, F. Chen and W. Cao, *FlatChem*, 2023, **39**, 100503.
127 P. Wu, T. You, Q. Ren, H. Xi, Q. Liu, F. Qin, H. Gu, Y. Wang, W. Yan and Y. Gao, *Nano Res.*, 2023, **16**, 1158–1164.
128 A. E. Vilian, S.-K. Hwang, G. Bhaskaran, M. Alhammadi, S. Kim, J. N. Tiwari, Y. S. Huh and Y.-K. Han, *Chem. Eng. J.*, 2023, **454**, 139980.
129 Q. Wang, J. Liu, S. Ren and Z. Zheng, Available at SSRN 4484602.
130 M. P. Thukkaram, A. Chakravorty, A. A. Mini, K. Ramesh, A. N. Grace and V. Raghavan, *Microchem. J.*, 2023, **193**, 109004.
131 Y. Zhao, J. Yang, Y. Wu, B. Huang, L. Xu, J. Yang, B. Liang and L. Han, *J. Hazard. Mater.*, 2023, **452**, 131265.
132 Z. Lu, K. Wei, H. Ma, R. Duan, M. Sun, P. Zou, J. Yin, X. Wang, Y. Wang and C. Wu, *Anal. Chim. Acta*, 2023, **1251**, 340983.
133 J. H. Kim, J. H. Shin, B. Park, C. H. Cho, Y. S. Huh, C.-H. Choi and J. P. Park, *J. Nanobiotechnol.*, 2023, **21**, 100.
134 M. Zhang, H. Liu and X. Wang, *J. Mater. Chem. B*, 2023, **11**, 1506–1522.
135 L. Tian, M. Jiang, M. Su, X. Cao, Q. Jiang, Q. Liu and C. Yu, *Microchem. J.*, 2023, **185**, 108172.
136 M. Wan, A. Jimu, H. Yang, J. Zhou, X. Dai, Y. Zheng, J. Ou, Y. Yang, J. Liu and L. Wang, *Microchem. J.*, 2023, **184**, 108180.
137 Y. Li, L. Zhang, M. Wu, G. Ma, M. Motlak and A. Mahdi, *Inorg. Chem. Commun.*, 2023, **155**, 111061.
138 S. J. Lee, D. H. Lee and W.-Y. Lee, *Microchem. J.*, 2023, **185**, 108216.
139 L. Tian, J. Zhang, H. Fan, Y. Zhang, Z. Wang, O. Oderinde, Y. Wang and J. Cui, *Anal. Biochem.*, 2023, **663**, 115028.
140 Z. Cai, B. Tu, R. Zhou, D. Xia, H. He, N. Gao, G. Chang and Y. He, *J. Electroanal. Chem.*, 2023, **928**, 117012.
141 Y. Zhao, Y. Xia, J. Zhang, H. Liu, Y. Yi and G. Zhu, *Microchem. J.*, 2023, **185**, 108207.
142 Z. Shi, C. Dai, P. Deng, X. Li, Y. Wu, J. Lv, C. Xiong, Y. Shuai, F. Zhang and D. Wang, *Sens. Actuators, B*, 2023, **383**, 133598.
143 S. Hroncekova, L. Lorencova, T. Bertok, M. Hires, E. Jane, M. Bučko, P. Kasak and J. Tkac, *J. Funct. Biomater.*, 2023, **14**, 161.
144 S. Guo, Y. Lin, Z. Lian, T. Zeng, L. Wang, R. Ye, B. Hong, Q. Liang, Q. Wu and J. Hu, *Microchem. J.*, 2023, **190**, 108656.
145 S. Ranjbari, M. Rezayi, R. Arefinia, S. H. Aghaee-Bakhtiari, B. Hatamluyi and A. Pasdar, *Talanta*, 2023, **255**, 124247.
146 L. Tian, J. Zhang, Y. Zhang, H. Fan, C. Liu, Y. Wang and J. Cui, *Sens. Actuators, B*, 2023, **390**, 133993.
147 H. Duan, Y. Wang, S.-Y. Tang, T.-H. Xiao, K. Goda and M. Li, *Sens. Actuators, B*, 2023, **380**, 133342.
148 X. Yu, S. Bai and L. Wang, *Front. Bioeng. Biotechnol.*, 2023, **11**, 1176046.
149 M. Bolourinezhad, M. Rezayi, Z. Meshkat, S. Soleimanpour, M. Mojarrad, S. H. Aghaee-Bakhtiari and S. M. Taghdisi, *Talanta*, 2023, 124804.
150 J. Tao, J. Han, W. Li, J. Cui, J. Li, X. Cao and H. Zhang, ResearchSquare, 2023, preprint, DOI: **10.21203/rs.3.rs-3036312/v1**.
151 X. Mi, H. Li and Y. Tu, *Chemosensors*, 2023, **11**, 157.
152 J. H. Kim, C. H. Cho, J. H. Shin, J. C. Yang, T. J. Park, J. Park and J. P. Park, *Anal. Chim. Acta*, 2023, **1251**, 341018.
153 T. Vessella, H. Zhang, Z. Zhou, F. Cui and H. S. Zhou, *Biosens. Bioelectron.*, 2023, **237**, 115512.
154 D. Li, Y. Ren, R. Chen, H. Wu, S. Zhuang and M. Zhang, *Microchim. Acta*, 2023, **190**, 284.
155 M.-H. Lee, K.-H. Liu, J. L. Thomas, C.-Y. Chen, C.-Y. Chen, C.-H. Yang and H.-Y. Lin, *Biosens. Bioelectron.*, 2022, **200**, 113930.
156 Y. Kong, Y. Zhu, J. Song, Q. Liu, L. Song, X. Fei and X. Li, *Food Chem.*, 2023, 136645.
157 L. Luo, X. Guo, X. Xi, T. Bao, Y. Li, Z. Wu, X. Zhang, S. Wang and W. Wen, *Sens. Actuators, B*, 2023, **381**, 133444.

158 D. Ren, X. Cheng, Q. Chen, G. Xu, F. Wei, J. Yang, J. Xu, L. Wang, Q. Hu and Y. Cen, *Microchem. J.*, 2023, **187**, 108397.
159 Z. Wu, D.-W. Sun, H. Pu and Q. Wei, *Talanta*, 2023, **253**, 124027.
160 Z. Wu, D.-W. Sun, H. Pu and Q. Wei, *Talanta*, 2023, **252**, 123773.
161 L. Du, Y. Chen, Y. Huang, S. Yan, S. Zhang and H. Dai, *Microchim. Acta*, 2023, **190**, 108.
162 T. Zhu, Q. Tang, Y. Zeng, S. Chen, Y. Yang, H. Wang, J. Chen, L. Guo and L. Li, *Spectrochim. Acta, Part A*, 2023, **293**, 122474.
163 Y. Liu, Y. Lv, W. Chen, X. Yang, X. Cheng, Z. Rong and S. Wang, *ACS Appl. Mater. Interfaces*, 2023, **15**, 35872–35883.
164 Z. Wang, Z. Zhang, H. Pan and D. Chang, *Anal. Biochem.*, 2023, **676**, 115233.
165 J. H. Choi, D. H. Lee and W.-Y. Lee, *J. Electroanal. Chem.*, 2023, **936**, 117389.
166 M. Wei, X. Du, D. Jiang, Y. Zhang, X. Shan, W. Wang, H. Shiigi and Z. Chen, *Biosens. Bioelectron.*, 2023, **236**, 115420.
167 M. Li, Z. Li, P. Wang and Q. Ma, *Biosens. Bioelectron.*, 2023, **228**, 115225.
168 W. Huang, S. Gao, W.-B. Liang, Y. Li, R. Yuan and D.-R. Xiao, *Biosens. Bioelectron.*, 2023, **220**, 114886.
169 Y. Li, P. Wang, Y. Nie and Q. Ma, *Microchem. J.*, 2023, 108957.
170 X. Wang, C. Hou, F. Zhang, J. Xia and Z. Wang, *Sens. Actuators, B*, 2023, **379**, 133229.
171 H. Zhou, L. You, J. Zhang, T. Hao, W. Gao, J. Xie, Y. Wu, Y. Hu, S. Wang and Z. Guo, *Sens. Actuators, B*, 2023, **390**, 134013.
172 G. Li, R. Singh, J. Guo, B. Zhang and S. Kumar, *Appl. Phys. Lett.*, 2023, **122**, 083701.
173 Y. Wang, Y. Hu, Q. Zeng, X. Chen, Y. Zhang, S. Zeng and H. Yang, Presented in part at CLEO: Fundamental Science, San Jose, CA, United States, May, 2023.
174 P. Thawany, A. Khanna, U. Tiwari and A. Deep, *Sci. Rep.*, 2023, **13**, 5297.
175 S. B. Saadatmand, M. J. H. N. Chemerkouh, V. Ahmadi and S. M. Hamidi, *J. Opt. Soc. Am. B*, 2023, **40**, 1–10.
176 W. Yang, R. Liu, J. Yan, Y. Xie, C. Wang, M. Jiang, P. Li and L. Du, *Biosens. Bioelectron.*, 2023, **235**, 115358.
177 S. Gunasekaran and W. Wang, Available at SSRN 4510487.
178 Y. Zheng, X. Cui, H. Yin, H. Zhang, L. Cao, L. Gao, Y. Zhou, P. Ju and S. Ai, *Anal. Chim. Acta*, 2023, **1251**, 341011.
179 R. A. Soomro, J. Kumar, R. R. Neiber, A. M. Alotaibi, S. F. Shaikh, N. Ahmed and A. Nafady, *Anal. Chim. Acta*, 2023, **1251**, 341016.
180 X. Ma, J. Kang, Y. Wu, C. Pang, S. Li, J. Li, Y. Xiong, J. Luo, M. Wang and Z. Xu, *Chem. Eng. J.*, 2023, 143888.
181 M.-l Huang, H.-m Deng, M.-l Cheng, H.-l Li, R. Yuan and S.-p Wei, *Sens. Actuators, B*, 2023, **394**, 134343.
182 C. Lai, B. Yan, R. Yuan, D. Chen, X. Wang, M. Wang, H. He and J. Tu, *RSC Adv.*, 2023, **13**, 16222–16229.
183 Y. Shi, T. Li, L. Zhao, Y. Liu, K. Ding, D. Li, P. He, D. Jiang, J. Liu and H. Zhou, *Biosens. Bioelectron.*, 2023, **230**, 115287.
184 Q. Zhou, Y. Liu, L. Wang, K. Wang, H. Chen, H. Zheng, Y. Zhou, Z. Hu, Z. Peng and J. Wan, *Chem. Eng. J.*, 2023, 143926.
185 D. Jiang, Y. Zhang, X. Du, L. Zhang, X. Shan, W. Wang, H. Shiigi and Z. Chen, *Chem. Commun.*, 2023, **59**, 1185–1188.
186 Y. Guo, X. Dai, Y. Zhang, S. Ma, L. Yang, Y. Bu and Y. Hao, *Anal. Chem.*, 2023, **95**, 7560–7568.
187 Z. Yang, L. Jiang, W. Zhao, B. Shi, X. Qu, Y. Zheng and P. Zhou, *Spectrochim. Acta, Part A*, 2023, **299**, 122843.
188 S. Zhi, J. Shi, A. Liang and Z. Jiang, *Talanta*, 2023, **251**, 123771.
189 Y. Zhou, Q. Chen, S. Zhong, H. Liu, K. Koh and H. Chen, *Biosens. Bioelectron.*, 2023, 115493.
190 Z. U. D. Babar, B. Della Ventura, R. Velotta and V. Iannotti, *RSC Adv.*, 2022, **12**, 19590–19610.
191 Y. Cheng, B. Jiang, S. Chaemchuen, F. Verpoort and Z. Kou, *Carbon Neutralization*, 2023, **2**, 213–234.
192 L. Yang, H. Guo, T. Hou, J. Zhang and F. Li, *Biosens. Bioelectron.*, 2023, **234**, 115346.
193 Z. Wu, D.-W. Sun, H. Pu, Q. Wei and X. Lin, *Food Chem.*, 2022, **372**, 131293.
194 G. Zamiri, A. A. Babadi, A. Numan, V. Chaudhary, R. Walvekar, M. Khalid and A. Khosla, *J. Electrochem. Soc.*, 2023, **170**, 037501.
195 A. Uzunoglu, E. G. Altuntas, H. H. Ipekci and O. Ozoglu, *Microchem. J.*, 2023, 108970.
196 Z. Wang, Z. Zhang, Y. Zhang, X. Xu, T. Shen, H. Pan and D. Chang, *Talanta*, 2023, 124848.
197 W. Feng, P. Xu, M. Wang, G. Wang, G. Li and A. Jing, *Micromachines*, 2023, **14**, 138.
198 L. Zhuang, Q. You, X. Su, Z. Chang, M. Ge, Q. Mei, L. Yang, W. Dong and L. Li, *Sensors*, 2023, **23**, 3508.
199 M. Wang, Z. Zhang, G. Li and A. Jing, *Micromachines*, 2023, **14**, 617.
200 G. Kim, Y. G. Li, Y. Seo, C. Baek, J.-H. Choi, H. Park, J. An, M. Lee, S. Noh and J. Min, *Biosens. Bioelectron.*, 2023, 115474.
201 S. Xiao, C. Cao, T. Ming, Y. Cao, Z. Yu and N. Gan, *J. Hazard. Mater.*, 2023, 131875.
202 W. Li, X. Bai, F. Xiao, J. Huang, X. Zeng, Q. Xu, Y. Song, X. Xu and H. Xu, *J. Hazard. Mater.*, 2023, 131823.
203 Y. Chen, Y. Gu, X. Yi, H. Huang, Y. Li, B. Yang, S. Guo and L. Bai, *Chem. Eng. J.*, 2023, **466**, 143112.
204 M. Duan, B. Li, Y. He, Y. Zhao, Y. Liu, B. Zou, Y. Liu, J. Chen, R. Dai and X. Li, *Talanta*, 2023, 125011.
205 A. Cui, P. Meng, J. Hu, H. Yang, Z. Yang, H. Li and Y. Sun, *Analyst*, 2023, **148**, 1058–1067.
206 H. Liu, S. Ma, G. Ning, R. Zhang, H. Liang, F. Liu, L. Xiao, L. Guo, Y. Zhang and C.-P. Li, *Talanta*, 2023, **258**, 124433.
207 C. Singh, S. Höfs, Z. Konthur, V.-D. Hodoroaba, J. R. Radnik, J. R. A. Schenk and R. J. Schneider, *ACS Appl. Eng. Mater.*, 2023, **1**, 495–507.
208 Z. Chen, C. Wu, Y. Yuan, Z. Xie, T. Li, H. Huang, S. Li, J. Deng, H. Lin and Z. Shi, *J. Nanobiotechnol.*, 2023, **21**, 141.
209 K. Ketabi, H. Soleimanjahi, A. Teimoori, B. Hatamluyi, M. Rezayi and Z. Meshkat, *Microchim. Acta*, 2023, **190**, 293.

210 M. Xin, J. Li, Z. Ma, L. Pan and Y. Shi, *Front. Chem.*, 2020, **8**, 297.
211 L. T. Yu, D. Z. Huang, X. Z. Wang, W. Yu and Y. A. Yue, *Phys. Chem. Chem. Phys.*, 2022, **24**, 25969–25978.
212 X. Li, J. Pan, Y. Wu, H. Xing, Z. An, Z. Shi, J. Lv, F. Zhang, J. Jiang and D. Wang, *Biosens. Bioelectron.*, 2023, **222**, 114945.
213 S. Zhang, S. S. Rana, T. Bhatta, G. B. Pradhan, S. Sharma, H. Song, S. Jeong and J. Y. Park, *Nano Energy*, 2023, **106**, 108110.
214 S. K. Kailasa, D. J. Joshi, J. R. Koduru and N. I. Malek, *J. Mol. Liq.*, 2021, **342**, 117524.
215 X. Jiang, A. V. Kuklin, A. Baev, Y. Ge, H. Ågren, H. Zhang and P. N. Prasad, *Phys. Rep.*, 2020, **848**, 1–58.
216 Z. Zheng, C. Guo, E. Wang, Z. He, T. Liang, T. Yang and X. Hou, *Inorg. Chem. Front.*, 2021, **9**, 2164–2182.
217 W. Meng, X. Liu, H. Song, Y. Xie, X. Shi, M. Dargusch, Z.-G. Chen, Z. Tang and S. Lu, *NanoToday*, 2021, **40**, 101273.

